Jet Reconstruction and Event-Background Fluctuations in Pb-Pb Collisions

Master Thesis

Markus Zimmermann

Institut für Kernphysik

Westfälische Wilhelms-Universität Münster

31. October 2012

Erster Gutachter: Prof. Dr. Johannes P. Wessels
Zweiter Gutachter: Dr. Christian Klein-Bösing

Contents

Contents

1. Introduction

The LHC (Large Hadron Collider) is a particle accelerator at CERN[1] where proton-proton (pp) and lead-lead (Pb-Pb) collisions take place. Six different experiments investigate the properties of matter. In Pb-Pb collisions, a new state of matter the so called QGP (Quark-Gluon Plasma) is created. This is investigated by several experiments, one of these being ALICE (A Large Ion Collider Experiment).

An important aspect of the analysis are jets, which are an accumulation of particles. They reflect the direction and transverse momentum of initially scattered particles. The measured transverse momentum of a jet has two contributions. One is from the fragmenting parton, and the other is the momentum of the background, which is particularly important in heavy-ion collisions. To only get the jet momentum, the median background has to be estimated for each event and than subtracted from the jets. This background subtraction already has been successfully done in [A$^+$12b]. Additional effects are statistical and region to region fluctuations in this background. These background fluctuations have been analyzed in [A$^+$12b] and can be quantified in a so called δp_T distribution.

In addition to this, detector effects complicate the energy estimation of the jets. The used detectors only have a restricted efficiency to detect a particle. This efficiency depends on the transverse momentum of the particle. Also, the detector setup influences the detection efficiency. These detector effects lead to a significant amount of missing charged particles in the events. To get the real value of a measured observable, it must be corrected for the detector effects. Another detector effect is the p_T resolution. The detector can only measure the value of the transverse momentum with a limited accuracy.

In this master thesis, the background fluctuations are corrected for the efficiency part of their detector effects. For this a new method, the HBOM method (based on [MOB11]), is explained and applied. This method does not require knowledge about correlations in the event. Only the measured data and the detector effects which should be corrected have to be known. First, only the standard deviation is corrected, and then a method is developed to also correct the whole δp_T distribution.

This thesis is structured as follows: In Chapter 2, a short introduction into the theoretical background of jets, their background in heavy-ion collisions and the HBOM method is given. The unfolding method for the correction of the jet spectrum is also explained. After a brief description of the LHC and ALICE in Chapter 3, the first simulations with the HBOM method are presented in Chapter 4. Different

---

[1]European Organization for Nuclear Research. The acronym CERN originally stood for Conseil Européen pour la Recherche Nucléaire.

configurations of the method are presented, and the one with the best results is chosen. Then in Chapter 5, this configuration is used to correct the detector effects of the δp_T spectrum for Pb-Pb data measured in 2010 and 2011. After the HBOM analysis, an alternative method to correct detector effects is shown. This method is the unfolding. It is applied to the jet spectrum in Chapter 6. Finally in Chapter 7, the results are summarized and an outlook is provided.

2. Theoretical Background

In this chapter, the theoretical background for the successive chapters is presented. First the underlying physics, the Standard Model of particle physics and the quark-gluon plasma, are explained. Among other things, jets are used to analyze these physical processes. For the jet analysis, it is important to learn something about the underlying event. This is shown in Sections 2.3 and 2.4.

After these sections, the detector effects which influence the previous analysis are discussed. The last two sections show two possibilities to correct a measurement for these detector effects. This thesis focuses on the HBOM method which is presented here.

2.1. The Standard Model
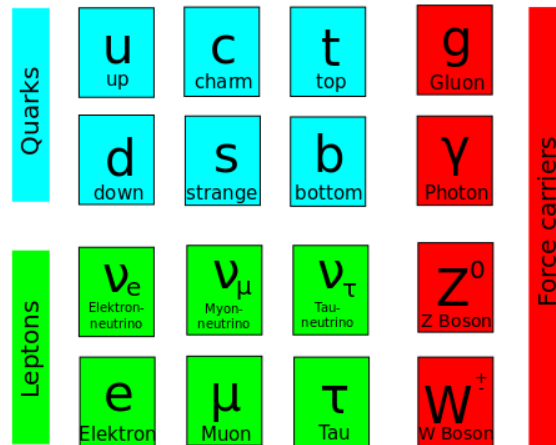
Figure 2.1.: Particles of the Standard Model of particle physics.

The Standard Model (SM) of particle physics describes the twelve currently known elementary particles and the gauge bosons of the strong, weak and electromagnetic interaction. The graviton, which is predicted as gauge boson for the gravitation, has not yet been proven and is not included. Figure 2.1 shows the three generations of quarks and leptons, as well as the gauge bosons [N+10].

Quarks and leptons are fermions with a spin of $\frac{1}{2}$. The force carriers are bosons with a spin of 1. There are three generations of quarks; each generation has two with different

electric charge. The up (u), charm (c) and top (t) quarks carry an electric charge of $+\frac{2}{3}e$, and down (d), strange (s) and bottom (b) carry $-\frac{1}{3}e$. In addition, the quarks have a color charge of red, blue or green. Antiquarks on the other hand have an anticolor and the negative charge of the quark ($-\frac{2}{3}e$ for ū, c̄, t̄ and $+\frac{1}{3}e$ for d̄, s̄, b̄). Like the quarks, the leptons have three generations. The generations are made up of an electron, muon or tau and their corresponding neutrinos. All six leptons interact weakly, and the electron, muon and tau additionally interact electromagnetically. They carry a charge of $-1\,e$.

The gauge bosons are the interaction particles for the different fundamental forces and couple to different charges. The photon is the mediator for the electromagnetic interaction. It couples to electric charges. Because their mass is zero, the interaction length is infinite. The weak force is mediated by the $W^{\pm}$ and Z bosons, which couple to the weak isospin. Due to their high mass of $80\,\mathrm{GeV}/c^2$ ($W^{\pm}$) and $91\,\mathrm{GeV}/c^2$ (Z), the interaction length of $\ll 1\,\mathrm{fm}$ is very short. The strong force is mediated by eight gluons, which carry a color and an anticolor. They couple to color charges, and due to their own color charge, gluons can couple to quarks and to other gluons. This is the reason for the self interaction of gluons. Although the gluons have a mass of zero, they only have an interaction length of a few fm. The reason for this is the confinement, which means that only colorless particles can be observed.

Until now only colorless particles have been observed with particle detectors. Either mesons made of a quark and an antiquark (a color and an anticolor) or baryons made of three quarks (with all three colors) or antiquarks (with all three anticolors) have been directly proven. Particles which carry an effective color charge hadronize before they reach the detector. The reason for this effect can be understood with the phenomenological potential of the strong interaction

$$V(r) = -\frac{4}{3}\frac{\alpha_S}{r} + kr. \tag{2.1}$$

Here α_S is the coupling constant of the strong interaction, and k represents the strength of the binding of two quarks. α_S depends on the momentum transfer in an interaction, for momentum transfers larger than $1\,\mathrm{GeV}/c$ it is below 1 and falls further with rising momentum transfer. The complete first term describes the Coulomb-like interaction, while the second describes the gluon self-interaction. Therefore, the parameter k in the second term is positive. Together, the potential rises for larger distances and diverges to minus infinity at $r = 0$. At very little distances $r \approx 0$ the coupling constant α_S tends to zero and the quarks have an asymptotic freedom [N$^+$10].

The reason for the hadronization of color charged particles is the second term of Equation 2.1. Because of this term, the potential rises linear with the distance of the color charges. For the separation of a quark-antiquark-pair, the minimal needed energy is the energy which is necessary to produce two new quarks. During the separation of the quarks, the energy in the binding rises until it is sufficient to produce a new quark-antiquark-pair. The newly produced quark forms a meson with the old antiquark and the produced antiquark another meson with the old quark. Because of this process, no free quarks can be observed. An analogy to this is a breaking elastic string which is
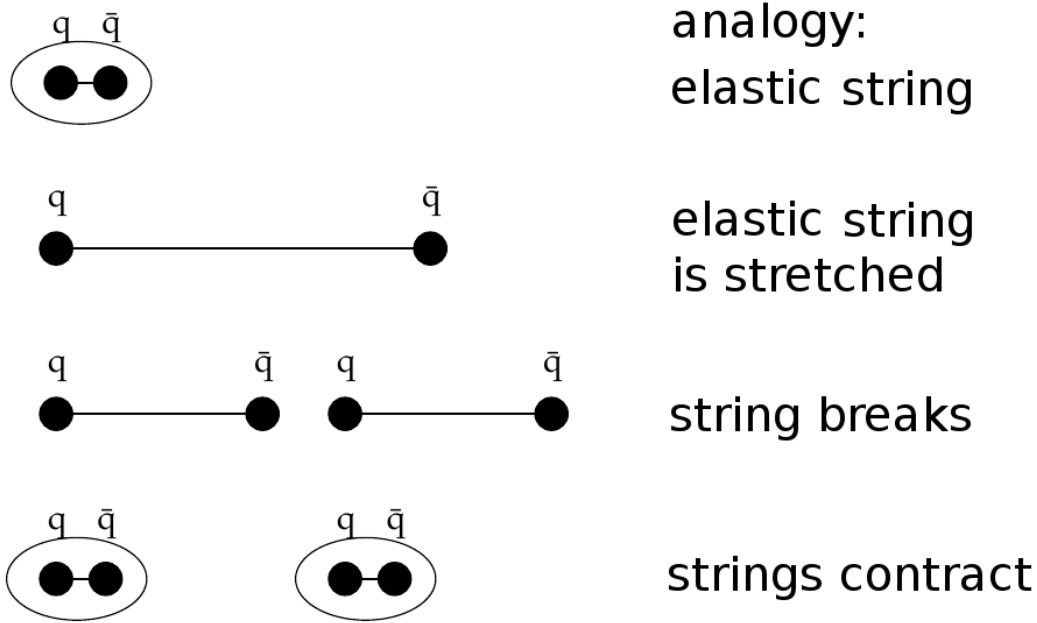
Figure 2.2.: Separation of the quarks in a meson. The right side describes the analogy of a breaking elastic string. Based on [Wei07].

shown in Figure 2.2. The string contains more energy the more it is stretched. When it breaks and the two components contract, this is the analogon to the two newly formed quarks [Wei07].

2.2. Quark-Gluon Plasma

In the last section, the confinement was introduced. Because of this, free quarks and gluons could not be observed. But it is still possible to study free quarks and gluons by heating matter up to very high temperatures and compressing it to very high densities. Lattice Quantum Chromo Dynamics (QCD) predicts a new state of matter for this high energies called Quark-Gluon Plasma (QGP). At lower energies, the matter forms a hadron gas, meaning that the quarks and gluons are arranged in hadrons. In this gas the most particles are the lightest hadrons the pions. The QCD phase diagram is shown in Figure 2.3. For high temperatures, the matter goes through a phase transition from the hadron gas into the QGP phase. The phase transition from the hadronic matter to the QGP phase is of the order of a crossover at the baryon chemical potential $\mu = 0$. Lattice QCD calculations predicted that there is no critical point in the transition from the hadron gas to the QGP [dFKP07]. Nevertheless, experiments are searching for the critical point. A color superconductor phase is predicted for high baryon chemical potential and low temperature. Up to now, this phase has not been observed and in
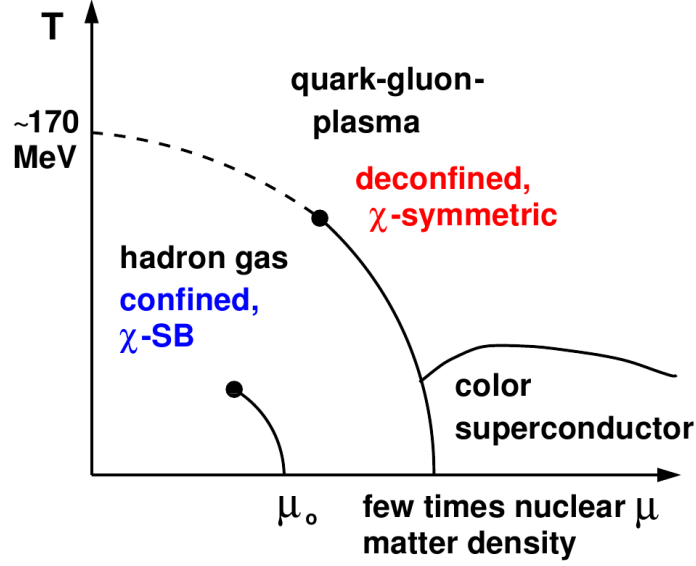
Figure 2.3.: The QCD phase diagramm depending on temperature (T) and baryon chemical potential (μ_b). At low μ and T, one sees the hadronic matter phase and at high T, the QGP phase. The color conductor phase is a theoretically predicted phase which has not yet been proven [AKB11].

collider experiments this phase is not reachable, because the colliding nuclei are heated up to high temperatures [AKB11].

Figure 2.4 shows the lattice QCD calculation at the phase transition from the hadron gas at low energies to the QGP at high energies. The hadron gas mainly consists of pions, so it has three degrees of freedom for the three different types of pions($\pi^{\pm}$ and π^0). In contrast, the QGP has 16 degrees of freedom for the gluons (8 gluons times 2 for the spin states) and $\frac{21}{2} n_f$ degrees of freedom for the quarks (3 colors times 2 for particle/antiparticle times 2 for the spin states times the number of flavors n_f times 7/8 for fermions). In the QGP, the quarks and gluons are no longer confined and can move quasi-freely, over a path length larger than the size of a pion or proton. Due to the increased degrees of freedom, the energy density rises at the transition from the pion gas to the QGP. For different numbers of flavors different energy densities in the QGP phase are reached. In Figure 2.4 calculations for 2 and 3 flavor states are presented. In both calculations, the phase transition can be recognized due to the strong rise of the energy density. Because of the different number of degrees of freedom in the QGP state, the reached energy density differs. Another little difference is the temperature at which the phase transition appears. The green curve shows the energy density of a $2 + 1$ flavor state. This means there are 2 light and 1 heavy flavor state [AKB11].

On the right side of the plot, arrows show the corresponding energy density of a Stefan-Boltzmann gas ϵ_{SB}/T^4. This value is the ideal limit, which is not reached at the shown temperatures in the QGP. Thus, the QGP cannot be interpreted as an ideal
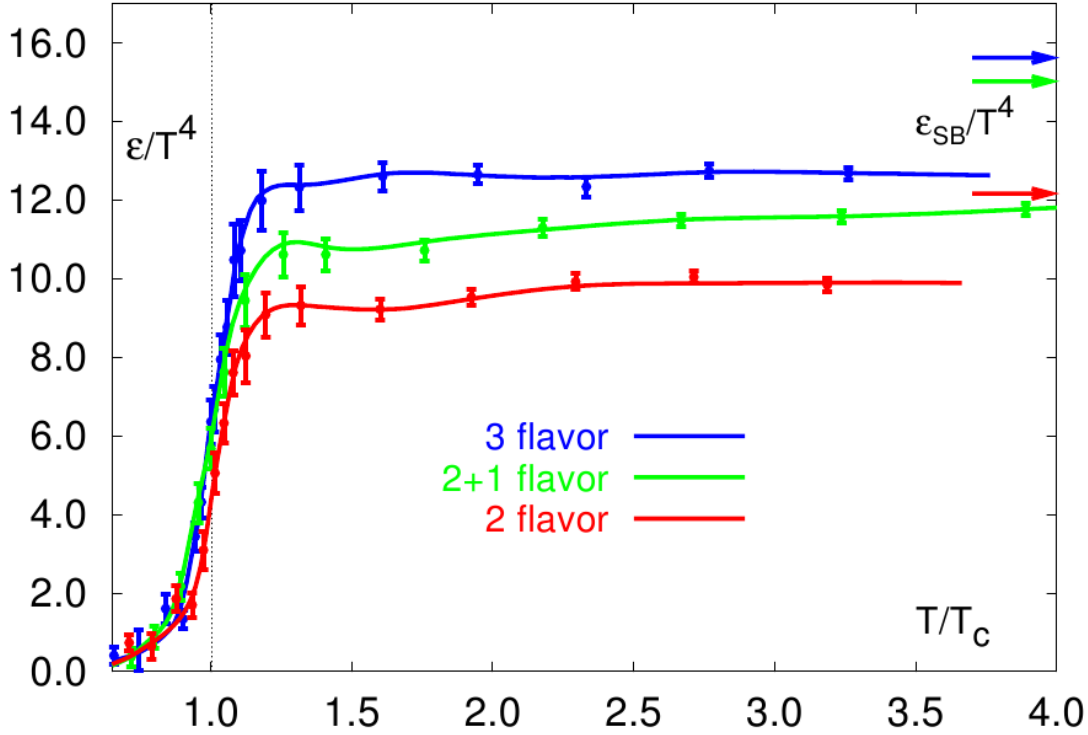
Figure 2.4.: The reduced energy density ϵ/T^4 in lattice QCD depending on the temperature in units of the critical temperature ($T_c = (173 \pm 15)\,\text{K}$) at baryon chemical potential of $\mu_b = 0$. The arrows on the right side indicate the Stefan-Boltzmann limit [Kar02].

gas.

It is assumed that a QGP existed shortly after the Big Bang in the early universe. The scientists working at the LHC are trying to reproduce the QGP in Pb-Pb collisions. For this purpose, the lead ions are collided with an energy up to $\sqrt{s_{NN}} = 5.54\,\text{TeV}$. This energy leads in the collision to the production of new matter states with high temperature and high energy density. The evolution of the different phases is shown in Figure 2.5. After the collision of nucleus A and nucleus B, a pre-equilibrium phase is generated in which the QGP is formed. The formation time τ_0 of the QGP is often assumed as $1\,\text{fm}/c$. This has a large uncertainty and only gives an upper limit to the formation time and with this, a lower limit to the energy density.

Due to the high pressure gradient, the QGP expands very quickly and cools down. Once the critical temperature T_c is reached the system becomes a hadron gas. In the mixed phase both the QGP and the hadron gas can exist simultaneously. In this phase, all particles still scatter inelastically until the temperature falls under the chemical freeze out temperature T_{ch}. At this temperature, the whole system is in the hadron gas phase. Now the particle distribution is fixed and only elastic scatterings are possible.
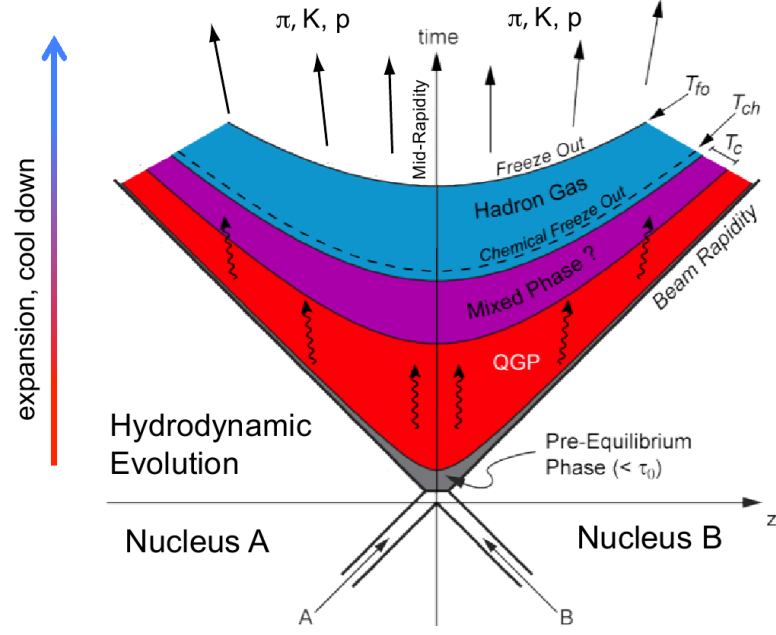
Figure 2.5.: Evolution of the QGP and subsequent phases [AKB11].

After the temperature falls under the kinetical freeze out temperature T_{fo}, the particles no longer scatter, and the kinetic distribution of the particles is also fixed [AKB11]. One possibility to detect the QGP is to measure jets. They are back to back placed in φ. In pp collisions, these jets can clearly be observed. The same is in principle possible for Pb-Pb jets. But if two particles do a hard scattering at the edge of the QGP, one scattered particle can go into the vacuum, and the other one has to go through the medium. The jet energy is determined by the first jet, which directly goes into the vacuum. The other jet, which is called the "quenched jet", looses energy in the QGP by medium-induced gluonstrahlung. This way it is possible that the second jet looses up to all its energy and vanishes in the measurement. In either case the second jet has significant less energy than the first jet.

The principle of producing a "quenched jet" is shown in Figure 2.6. While the upper jet radiates only a few gluons and hadronizes, the lower jet radiates many gluons due to the medium induced gluonstrahlung before it hadronizes [AKB11].

2.3. Jets

The color confinement of quarks and gluons has already been explained in the last section. On the way from the collision to the detector, the quarks and gluons radiate gluons and form quark-antiquark-pairs. This effect is called fragmentation. When the energy drops below the critical temperature T_c, the particles form hadrons. This process is called hadronization. Instead of quarks and gluons, only these hadrons can be
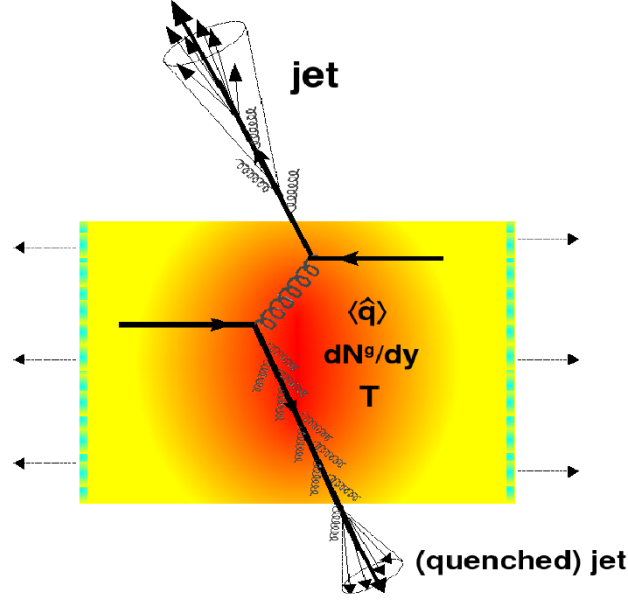
Figure 2.6.: "Jet quenching" in a Pb-Pb collision. Two quarks do a hard scattering. One goes into the vacuum and radiates a few gluons before it hadronizes. The other one goes through the QGP, suffers energy loss by medium-induced gluonstrahlung and hadronizes into the quenched Jet [d'E09].

detected. To get information about the primary scattered particles, the fragmentation can be measured, and the transverse momentum can be reconstructed.

For this purpose, jets are build up from the detected particles. A jet is an accumulation of particles in a defined area in the $\eta - \varphi$ plane, where η is the pseudo-rapidity[1] and φ the polar angle. In principle there are two groups of algorithm to find jets, the so called jet-finder.

One group of jet-finder works on the basis of cone algorithms. A seed particle is chosen, and a cone with radius R is put around this seed particle. The transverse momentum of all particles within the cone is summed up, and a p_T weighted average of η and φ is taken as the new seed for the next iteration. This procedure is iterated until the direction of the seed changes between two iterations less then a predefined value. All particles in this last cone form a jet.

Another group of jet-finder is the sequential recombination algorithms. A distance between two particles d_{ij} and a distance for one particle to the beam d_{iB} is defined. These distances are defined similarly to the R in the cone algorithms, with p_T depending weighting factors. For each particle, the distance to all other particles and to the beam

---

[1]The pseudo-rapidity $\eta = -\ln\left[\tan\frac{\theta}{2}\right]$ is a coordinate which describes the angle θ between the particle momentum and the beam axis. It is a simplification of the rapidity y for mass $m = 0$ which is invariant under Lorentz transformation and depends on the particle momentum p_T and the particle mass m.

is calculated. Then the lowest distance is chosen. If it is a d_{ij}, the particles are combined to one pseudo-particle and new distances for this particle are calculated. Otherwise the pseudo-particle is removed from the event and marked as a jet. This procedure is repeated until no particles are left. One of this algorithms is the k_t algorithm, which is used for the background estimation in this thesis. Another jet-finder is the anti k_t algorithm, which is used in the measurement of the jet spectrum for the unfolding. The difference between this algorithms is the definition of the distances:

$$k_t : d_{ij} = min(p_{T,i}^2, p_{T,j}^2)\frac{\Delta R_{ij}^2}{R^2} \tag{2.2}$$

$$k_t : d_{iB} = p_{T,i}^2 \tag{2.3}$$

$$\text{anti } k_t : d_{ij} = min(p_{T,i}^{-2}, p_{T,j}^{-2})\frac{\Delta R_{ij}^2}{R^2} \tag{2.4}$$

$$\text{anti } k_t : d_{iB} = p_{T,i}^{-2} \tag{2.5}$$

This leads to a different sequence of particle recombination. For the k_t algorithm, the low p_T particles are combined first, while the anti k_t combines the high p_T particles first.

A found jet represents the transverse momentum of a scattered quark or gluon. In Pb-Pb collisions, different observables like the number of particles or the energy distribution in the jets may give further information. The presented information as well as further information about the jet-finders can be found in [Zim10] and [Sal09]. Especially in Pb-Pb collisions there is a background below the jet, whose origin does not belong to the scattered particle, but comes from other nuclear reactions within the collision. To get the true energy of the jet, the background energy has to be subtracted. The way the background is calculated and subtracted is described in the next chapter.

2.4. Background Subtraction and Fluctuations

The background subtraction and the fluctuations of this background are explained in the following section [A$^+$12b]. In the simulations and data analysis, the sequential recombination algorithm k_t from the FastJet package [CS06] is used.

For every charged-particle jet, the background has to be determined and subtracted to get the real jet energy. The background estimation is done for each event. First, a transverse momentum cutoff of $p_{T,min} = 0.15\,\text{GeV}/c$ is applied to all particles. This means all particle with a momentum less than this cut are rejected from the analysis. With the k_t algorithm, background clusters are determined out of a list of particles if they are within the track acceptance of $|\eta| < 0.9$. Clusters within the track acceptance of $|\eta| < 0.9$ can be reconstructed with a radius of $R = 0.4$ to jets within $|\eta| < 0.5$, which is a commonly used acceptance for jets in ALICE. Only these clusters are considered in the background estimation. Then the p_T of the particles in one cluster is summed up to the reconstructed transverse momentum $p_{T,rec}$. To reduce the influence of real jets onto the background estimation, the two leading $p_{T,rec}$ clusters are removed from the list.
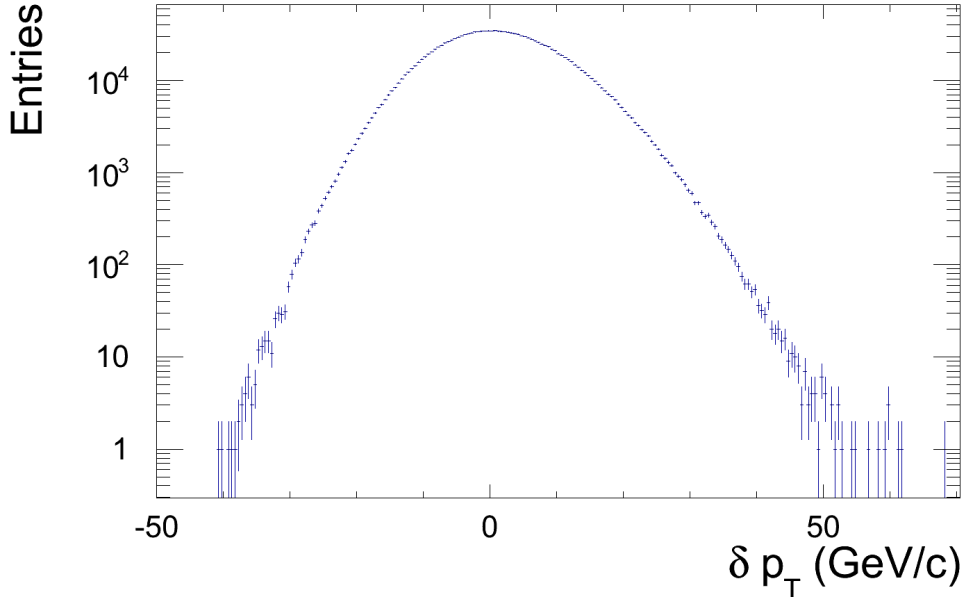
Figure 2.7.: Simulated δp_T spectrum. On the left side the spectrum has a Gaussian shape, on the right side it has an extra tail of jets on top. $1.6 \cdot 10^6$ events are simulated for the shown spectrum.

For this, the leading cluster is the one with the highest $p_{T,rec}$. Then the background $\rho = p_{T,rec}/A^{rec}$ is calculated by dividing the momentum $p_{T,rec}$ of each cluster by the area A^{rec} of the jet. The median of all determined backgrounds is taken as event background ρ.

To get further information about the fluctuations of the background, random cones are placed in the measured events. This means a cone of radius $R = 0.4$ is placed randomly in $|\eta| < 0.5$ and φ. Then the transverse momentum $p_{T,rec}$ within the cone is calculated, and the background $p_{T,back} = \rho \cdot A$ is subtracted to get the difference

$$\delta p_T = p_{T,rec} - p_{T,back}. \tag{2.6}$$

For the random cones the area is always the same with $A = \pi R^2$. To get a minimum bias result, only one random cone per event is placed.

Figure 2.7 shows a δp_T distribution for $1.6 \cdot 10^6$ simulated events with one random cone each. In section 4.1, the simulation is explained in detail. On the left side of the distribution, a Gaussian shape is clearly observable. On the right side at positive δp_T, the distribution shows a longer tail. In the simulation the particle p_T dependence of real events is used as input spectrum. The tail on the right side is produced by high p_T particles. The simulation places all particles with random η and φ. Therefore, there are no jet correlation in simulated events which would produce an even bigger tail, which persists in real events.

A way to describe the background fluctuations is to determine the standard deviation

$\sigma(\delta p_T)$. Different sources contribute to these fluctuations. The first basic one is the purely random fluctuation of the track p_T and number of tracks N_A in the cone. This dependence was developed by [A$^+$12b]

$$\sigma(\delta p_T) = \sqrt{N_A \cdot \sigma^2(p_T) + N_A \cdot \langle p_T \rangle}. \tag{2.7}$$

Here $\sigma(p_T)$ is the standard deviation and $\langle p_T \rangle$ the average p_T of the track p_T spectrum. Besides this fluctuation, there are also uncorrelated non-Poissonian (NP) fluctuations. These could be region-to-region variations induced e.g. due to collective flow. Knowing the standard deviation of these processes $\sigma_{\mathrm{NP}}(N_A)$, the standard deviation of the fluctuations can be calculated following [A$^+$12b]

$$\sigma(\delta p_T) = \sqrt{N_A \cdot \sigma^2(p_T) + (N_A + \sigma_{NP}^2(N_A)) \cdot \langle p_T \rangle}. \tag{2.8}$$

Figure 2.8 shows the $\sigma(\delta p_T)$ for different contributing fluctuation sources. The red circles show the background determined by the random cones. It has been tried to estimate the background more precisely by reducing the part of the jets on the δp_T determination. To do this, the random cones avoid covering the leading jet in the event (blue triangles). The collective fluctuations like the flow are destroyed by randomizing the track positions in η and φ (black triangles) [A$^+$12b].
In these results, the detector effects are still present. One part of the detector effects is the detection efficiency. This thesis provides a method of correcting the $\sigma(\delta p_T)$ and even the whole δp_T distribution to almost full detection efficiency.

2.5. Detector Effects

Each detector determines an observable only with a certain uncertainty and has a limited efficiency to detect particles. Low momentum charged particles do not reach the detectors behind the ITS, each material slows down the particles, and particles could miss the detection volume. Besides this low momentum charged particles, also particles with higher moments are not detected. They are called the missing charged particles. Monte Carlo simulations determined the detection efficiency in pp collisions for different p_T. To adapt this to Pb-Pb collisions, a constant efficiency of $4\,\%$ has to be subtracted [Ver12]

$$\epsilon_{Pb-Pb} = \epsilon_{pp} - 0.04. \tag{2.9}$$

Figure 2.9 shows the efficiency of detecting a particle in a Pb-Pb collision depending on the particle momentum p_T. In addition to this detection efficiency, the efficiency of detecting a particle at a given φ has to be considered. Between two detector segments is always a little area in which no particles could be detected. Because of the magnetic field in which the detector is placed (cf. Section 3.2.1), all charged particles follow a curved trajectory. Thus, the detection efficiency at the detector borders is also p_T dependent. Another φ dependent problem are dead sectors in the detectors. This could be because parts of the detector had to be operated at a low voltage, which may lead
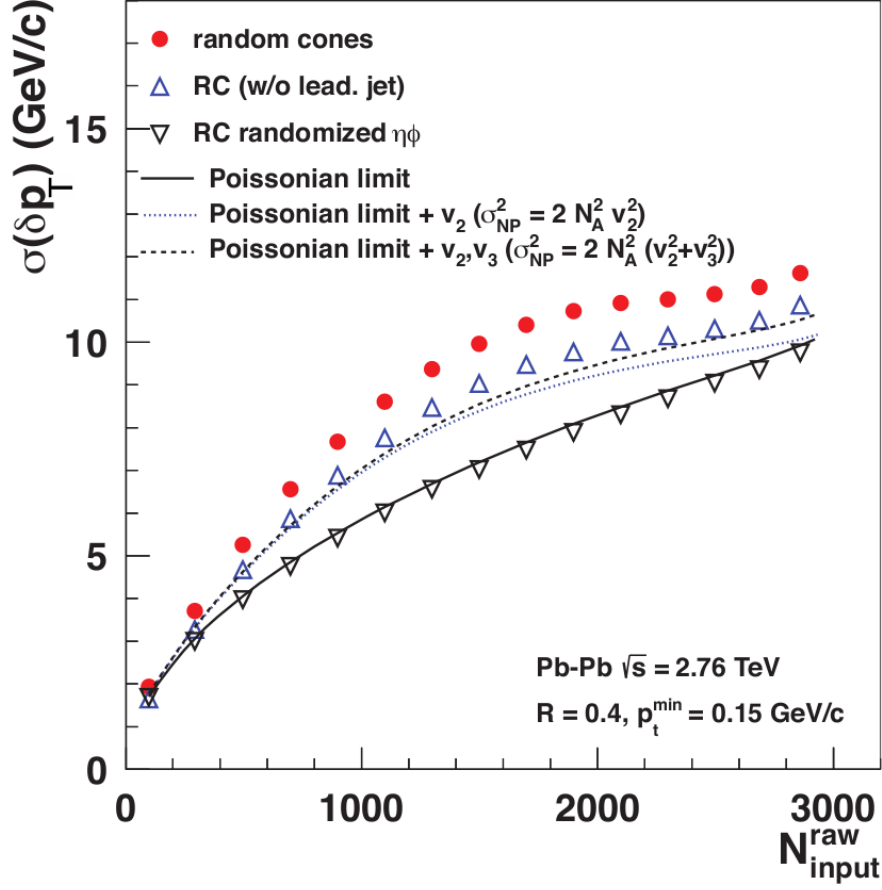
Figure 2.8.: Standard deviation of the δp_T distribution depending on the multiplicity $N_{\mathrm{input}}^{\mathrm{raw}}$ for different background contributions. The black triangles show the standard deviation for randomized events. This means all particles in the events got a new random η and φ. By doing this, all jet correlations in the event are destroyed. For the blue triangles in each event the leading jet is excluded from the background calculation. This reduces the jet part of the tail on the right side of the δp_T distribution. The standard deviation of the measured δp_T distribution is shown in red circles [A⁺12b]. In this thesis a centrality of $0 - 10\%$ is used which corresponds to a mean multiplicity of $N_{\mathrm{input}}^{\mathrm{raw}} = 2000$.
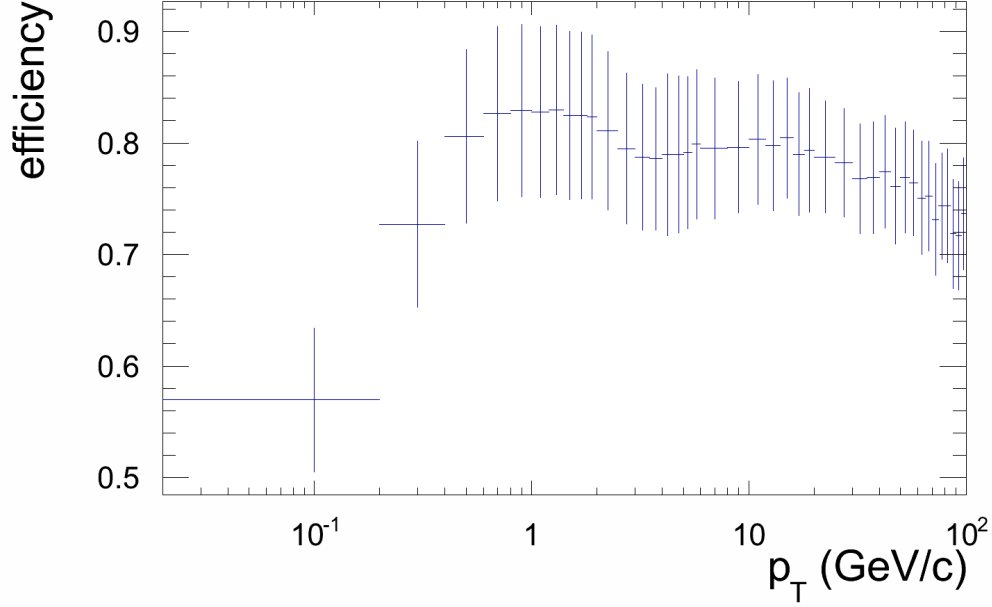
Figure 2.9.: Single track efficiency ϵ_{Pb-Pb} to detect a particle in a Pb-Pb collision depending on the transverse momentum p_T of the particle. These values are determined from Monte Carlo simulations. The spectrum is available in AliRoot at OADB/PWGJE/HBOM/fastMCInput_LHC10h_120827.root in the revision 58316.

to the exclusion of some tracks by offline analysis cuts, or because parts of the detector are not installed until now. The φ dependent efficiency is shown in Figure 2.10 in relative units to the p_T dependent efficiency in Figure 2.10.

To get the detection efficiency of a particle in a Pb-Pb event the single track efficiency and the φ efficiency have to be multiplied

$$\epsilon = \epsilon_{Pb-Pb} \cdot \epsilon_\varphi. \tag{2.10}$$

2.6. HBOM Method

The Hit Backspace Once More (HBOM) method is derived from [MOB11]. It is designed to correct observables of a measurement to a detector effect of almost zero. The initial situation is a measured observable $x(0)$ which contains detector effects. In the application of the HBOM method in this thesis, the observable is determined out of a distribution which bases on many particle collisions. Then the efficiencies to detect a particle with a certain p_T and position in the event have to be known from data analysis and Monte Carlo simulations (cf. Section 2.5). But this can be generalized to a common detection efficiency for other applications.

With the known detector efficiencies, fast detector simulations are done. The "fast"
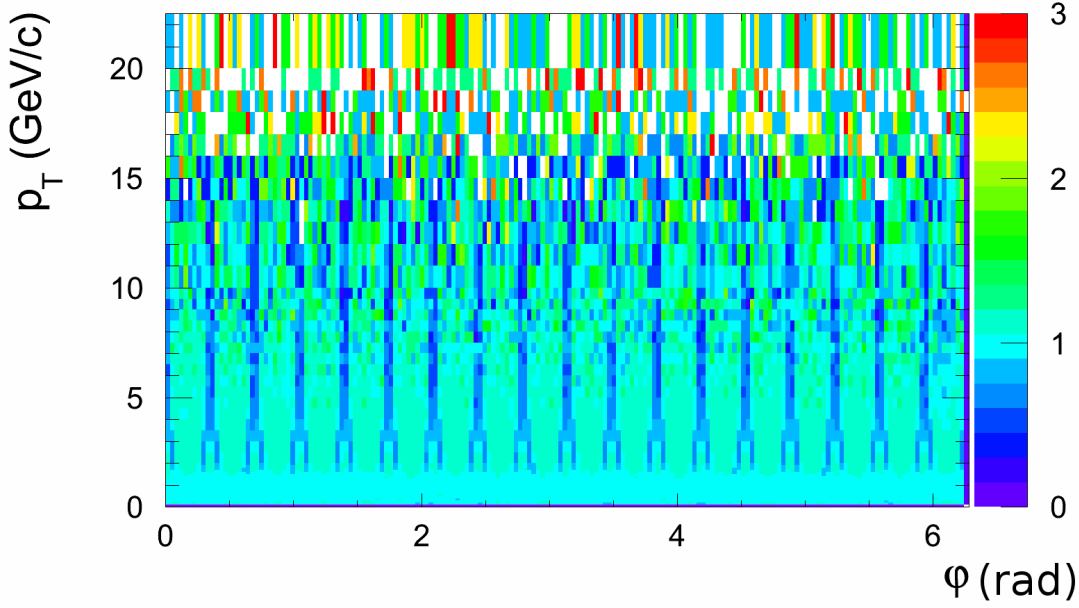
Figure 2.10.: Efficiency ϵ_φ to detect a particle in a Pb-Pb collision depending on φ and the transverse momentum p_T of the particle. At low p_T 18 areas of low efficiency are observable. These are named efficiency holes and are caused by the segmentation of the TPC. The values are determined in relative units so that they could be multiplied with the single track efficiency to get the detection efficiency. This efficiency is calculated with 2010 Pb-Pb data [KBa].

means there are no full detector simulations but an efficiency check for all particles. For every particle in an event, the efficiency to detect this particle ϵ is determined according to its p_T and φ. If a random number x is larger than the detection probability $x > \epsilon$, the particle is removed from the event. After doing this for all particles in all events, $x(1)$ can be determined.

This is called a detector hit and can be repeated several times. After each detector hit, the remaining particles are used as input to the next detector hit. In the second detector hit $x(2)$ is created and this way up to $x(N)$ can be calculated. For this thesis $N = 4$ is chosen as maximum for the application of the HBOM method. In principle, an arbitrary number of detector hits can be done. However, the method only works well if the efficiency is not near 0. After the detector hits there have to be enough particles left to make a meaningful analysis of the observable, which should be corrected for the detector effects.

An alternative approach to get $x(i)$ is to use always the particles of the measured events (used for $x(0)$) as input. Than the detection efficiency of a particle switches to ϵ^i. Both approaches lead to the almost same correction of the detector efficiencies. The differences are shown in Section 4.4.
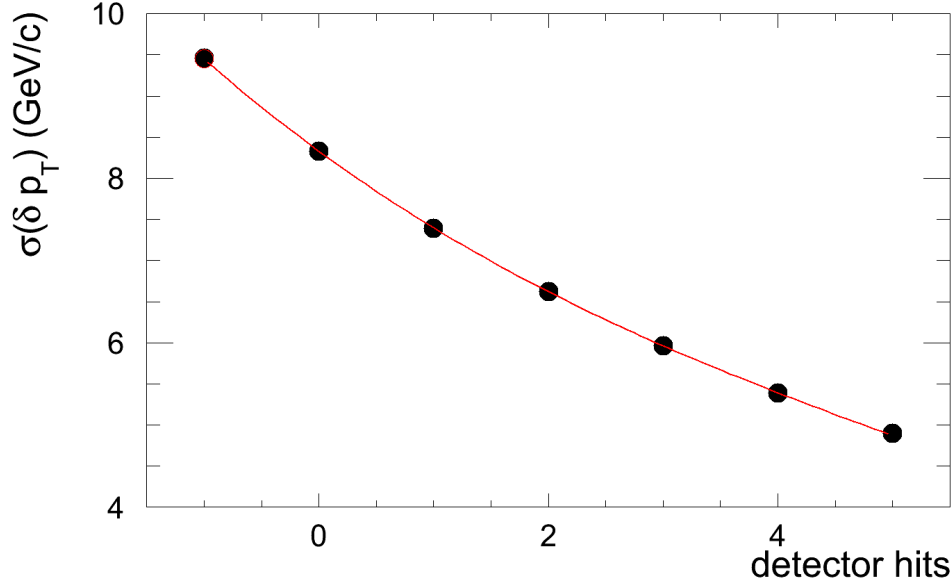
Figure 2.11.: HBOM Method for $\sigma(\delta p_T)$ up to 5 detector hits. The 3rd order polynomial is fitted to the points 0 to 4. Overall $1.6 \cdot 10^6$ events are simulated.

All determined points x(i) are plotted against the detector hits i in Figure 2.11. A polynomial of 3rd order is fitted to the points between 0 and 4 detector hits. An extrapolation of the fit to -1 detector hits provides the detector effect corrected observable. The statistical uncertainty is calculated with the Covariance matrix of the fit. The systematical uncertainty is described in Section 4.5. As a quality check, the point at 5 detector hits is also calculated, but it is not used for the fit.

2.7. Unfolding

In ALICE, jets are used to build up a jet spectrum. It shows the differential number of produced jets per p_T and η and is normalized by the number of events N_{evt} and the number of binary collisions N_{Coll}. The latter is determined out of the Glauber model. There the collision of two lead nuclei is considered as many collisions of protons which are superposed. This number of proton collision is N_{Coll}. Like the observables in the δp_T spectrum (which will be corrected with the HBOM method), the jet spectrum should also be corrected for the detector effects. However, the HBOM method corrects only the influence of the detector efficiencies. A wrong estimation of the background would not be considered. Instead of the HBOM method, the unfolding is used for the correction of the jet spectrum.

The basis for the unfolding process is the following equation

$$\vec{M} = \mathbf{R} \cdot \vec{T}. \tag{2.11}$$

The measured spectrum $\vec{M}$ is determined by the "true" spectrum $\vec{T}$ multiplied by the response matrix $\mathbf{R}$. The simple inversion of $\mathbf{R}$ is not always possible and if it is possible, the solution of the multiplication with $\vec{M}$ fluctuates strongly due to statistical uncertainties in the response and the measured spectrum. Instead of this, a guessed unfolded spectrum $\vec{U}$ is assumed and multiplied with the response matrix $\mathbf{R}$. Then the result, the folded spectrum $\vec{F} = \mathbf{R} \cdot \vec{U}$, is compared to the measured spectrum. If this spectrum agrees, the unfolded spectrum is the detector corrected spectrum. A measured spectrum is expected to be smooth, so the unfolding process requires a certain level of continuity.

There are some implementations of the unfolding. One of these is the χ^2 minimization method:

$$\chi^2(U) = \sum_m \left(\frac{M_m - \sum_t R_{mt} U_t}{e_m} \right)^2 + \beta P(U) \tag{2.12}$$

It is defined as the deviation of the folded spectrum from the measured one, plus a regularization term which only depends on the unfolded spectrum and prefers continuity. Here e_m is the error of the m-th bin in the measured spectrum, β is the strength of the regularization and $P(U)$ is the regularization term itself. For every unfolding process, β has to be tuned to be sure the regularization term does not dominate the unfolding. Further information about the unfolding process can be found in [Zim10] and [Ver12].

3. The LHC and the ALICE Experiment

The analysis of this thesis is based on data from the ALICE experiment located at the LHC. In this chapter, a brief description of the Large Hadron Collider (LHC) and its experiments is given. A more precise view is spent on ALICE and its subdetectors.

3.1. The Large Hadron Collider

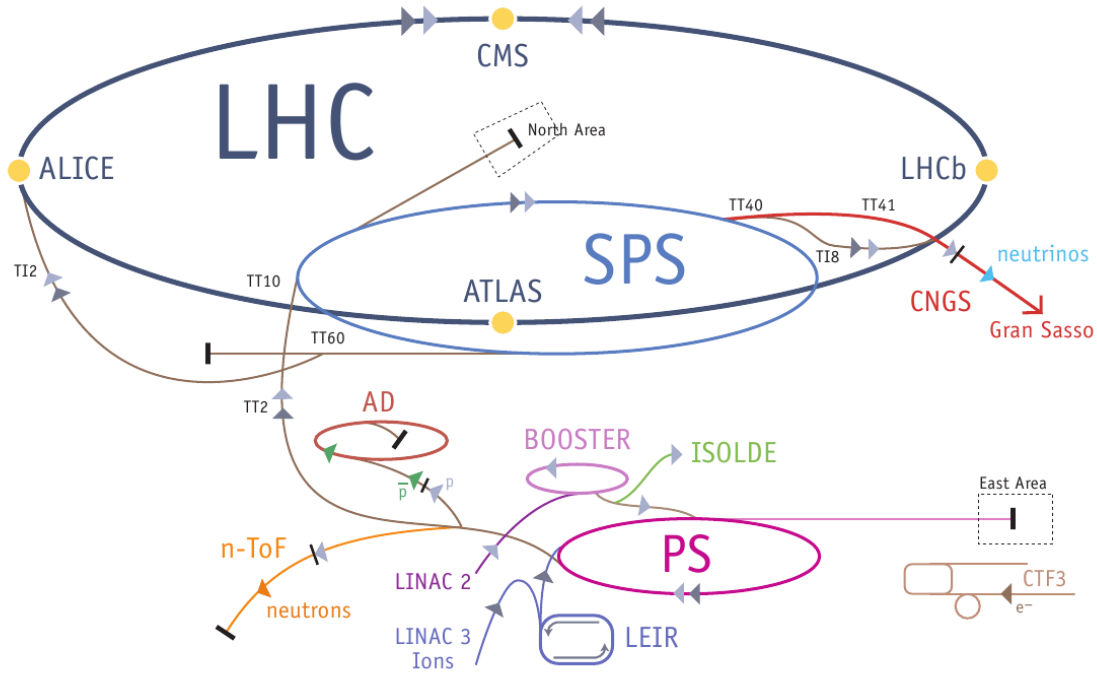Figure 3.1.: Schematic view of the LHC and its pre-accelerators. The yellow points represent the four big experiments at the LHC [Lef09].

With his circumference of approximately 27 km, the LHC is the biggest collider in the world. It is built at the European Organisation for Nuclear Research (CERN) near Geneva.
Figure 3.1 shows the acceleration steps for the LHC. The protons are accelerated in

the LINAC2, PS booster, PS and SPS. However, the lead-ions are accelerated in the LINAC3, LEIR, PS and SPS. From SPS the particles are injected into the LHC.

The collision energy of 8 TeV for the proton-proton-beam and 574 TeV for the lead-ion-beam is the highest energy which has been reached up to now. The designed maximum collision energy is 14 TeV for protons and 1150 TeV for lead. To reach these energies, the LHC uses 8 cavities per beam. Each cavity produces an accelerating field of 5 MV/m. The beam pipes are surrounded by 9593 magnets. 1232 are main dipole magnets with a peak magnetic dipole field of 8.33 T to keep the particles on the accelerator ring. To produce this strong magnetic field, the magnets are cooled down to 1.9 K by superfluid helium.

There are up to 2808 bunches in the beam pipes, each with $1.1 \cdot 10^{11}$ protons. At the designed luminosity[1] of $\mathcal{L} = 10^{34}\,\mathrm{cm}^{-2}\mathrm{s}^{-1}$ these bunches have a bunch spacing of 25 ns (this is equal to a distance of 7 m). A bunch crossing is only possible at the four interaction points of the big experiments. During one single bunch crossing ≈ 20 protons will collide. With 30 million bunch crossings per second, this leads to 60 million particle collisions per second. This collision rate is used in the ATLAS and CMS experiment. In ALICE, only a lower collision rate could be read out and one bunch is only collided with a satellite of another bunch. But this is only possible as long as not all bunches are filled. If all bunches are filled there are no more sattelite bunches. So the collisions of bunches with sattelites is done currently but will not be possible in the future.

The LHC is used for four big and two small experiments. The positions of the four bigger experiments ALICE, ATLAS, CMS and LHCb are shown in Figure 3.1. The smaller ones are LHCf near ATLAS, and TOTEM near CMS. In the following sections a very short description of each experiment is given [Lef09].

ALICE - A Large Ion Collider Experiment

ALICE was built to study heavy-ion collisions. It investigates the properties of the QGP. Further details are explained in Section 3.2.

ATLAS - A Toroidal LHC ApparatuS

ATLAS is a general-purpose pp detector which studies the widest possible range of physics. Among other things, it searches for the Higgs boson, the supersymmetry (SUSY) and extra dimensions. Additionally, it has a heavy-ion program. The detector consists of eight 25 m long superconducting magnet coils. This is the largest-volume collider-detector, which ever has been built.

Recently this detector and CMS discovered a particle which is consistent a with Higgs boson at 125 GeV [Rel].

---

[1] In accelerator physics, the luminosity is defined by $\mathcal{L} = fnN^2/A$ where f is the rotational frequency, n the number of bunches, N the number of particles per bunch and A the beam cross-section.

CMS - Compact Muon Solenoid

Like ATLAS, CMS is a general-purpose pp detector with the same physics goals but a different design. The experiment is built around a huge superconducting solenoid, which generates a magnetic field of 4 T.

LHCb - Large Hadron Collider beauty

LHCb studies the asymmetry between matter and antimatter in the production of B-particles. This is done by a series of subdetectors, which mainly detect particles in forward rapidity.

LHCf - Large Hadron Collider forward

The LHCf experiment is a small experiment 140 m away from the ATLAS collision point. It measures particles produced very close to the direction of the beam. The goal is to test models which are used to estimate the primary energy of the ultra high-energy cosmic rays.

TOTEM - TOTal Elastic and diffractive cross section Measurement

TOTEM is placed near the collision point of CMS and studies the effective size or cross-section of the proton at LHC. To do this, TOTEM has to measure particles produced close to the beam pipe. This also provides information about the luminosity.

3.2. ALICE

ALICE is a heavy-ion experiment located at the interaction Point 2 (P2) in St. Genis-Pouilly in France. It was built to study the physics of the QGP by measuring particles which are produced in lead-lead (Pb-Pb) and proton-proton (pp) collisions. Only the Pb-Pb collisions create the QGP, but the comparison to pp measurements is essential as reference.

In particular, the detectors of ALICE identify and track the produced particles with a transverse momentum p_T from $\sim 100\,\mathrm{MeV}/c$ up to $\sim 100\,\mathrm{GeV}/c$. The transverse momentum is defined as the momentum perpendicular to the beam direction. The particle detection is designed to be done in an environment of up to 8000 charged particles per rapidity unit at mid-rapidity. In the following section, the subdetectors of ALICE are shortly described [Lef09].

a. ITS SPD
b. ITS SDD
c. ITS SSD
d. V0 and T0
e. FMD
f. Beam pipe

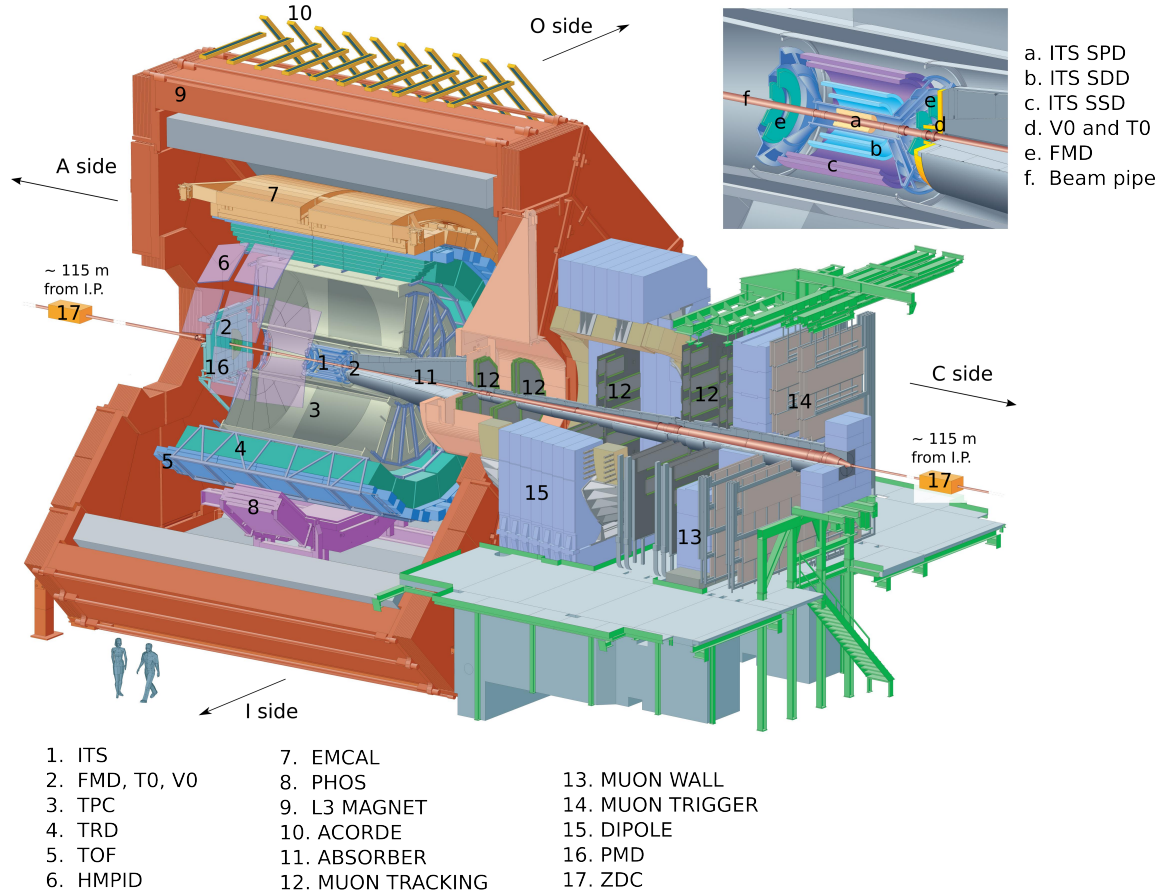|		
1. ITS	7. EMCAL	
2. FMD, T0, V0	8. PHOS	13. MUON WALL
3. TPC	9. L3 MAGNET	14. MUON TRIGGER
4. TRD	10. ACORDE	15. DIPOLE
5. TOF	11. ABSORBER	16. PMD
6. HMPID	12. MUON TRACKING	17. ZDC

Figure 3.2.: Schematic view of ALICE [A$^+$08]. The detailed view on the upper right
side shows the inner detectors.

3.2.1. Subdetectors of ALICE

In Figure 3.2, the ALICE detector is shown. The subdetectors are arranged in three
different areas: the central barrel, the forward detectors and the muon spectrometer.
Between the collision point and the muon spectrometer, an absorber is placed to shield
the muon spectrometer from the produced hadrons and photons.

Around the beam pipe, which has a radius of 3 cm, the innermost detector is the Inner
Tracking System (ITS), which consists of six cylindrical detector layers located between
4 and 44 cm. It covers $|\eta| < 0.9$ in full azimuth and is designed to reconstruct the
primary vertex with a resolution better than 100 μm. Secondary vertices should also
be detected. For low momentum particles ($<$100 MeV/c), only the ITS identifies and
tracks these particles. The identification is done by energy loss measurement in the
outer four layers [C$^+$04].

The Time Projection Chamber (TPC) is located outside of the ITS. It is the biggest
TPC ever built and the main tracking detector for ALICE. It observes the charged

particles of the events. Within the pseudo-rapidity $|\eta| < 0.9$ and full azimuth, the TPC reaches a good momentum resolution up to $100\,\text{GeV}/c$ and higher. The full readout of the TPC takes over $90\,\mu s$. This long readout is only done when the event is interesting. Therefore, triggers are needed to decide which events should be read out and which should not. For example, beam-gas collisions are rejected by triggers. In these beam-gas collisions, a beam particle collides with a particle from the residual gas. Another application of triggers is the centrality selection. For some analysis, only central collisions with a high multiplicity are preferred [C+04].

The next outer detector is the Transition Radiation Detector (TRD), which is placed between 2.9 and $3.7\,\text{m}$ radial distance to the primary vertex. It covers $|\eta| < 0.9$ and is used to distinguish electrons from pions for $p_T > 1\,\text{GeV}/c$. Furthermore, the TRD can provide a trigger signal for high p_T hadrons and electrons [C+04].

Around the TRD, the Time Of Flight (TOF) Detector is located between the radii 3.7 and $4.0\,\text{m}$. Like the other central barrel detectors, the TOF covers $|\eta| < 0.9$ and full azimuth. It measures the time of flight between the interaction point and the surface of the detector. This leads between 0.3 and $3.5\,\text{GeV}/c$ to the particle identification. Together with ITS and TPC, an event-by-event particle identification is achieved up to $2.5\,\text{GeV}/c$ for pions and kaons and up to $4.0\,\text{GeV}/c$ for protons [C+04].

Above the TOF at the two o'clock position, the High Momentum Particle Identification Detector (HMPID) is positioned. It covers a pseudo-rapidity $|\eta| < 0.6$ and an azimuthal area of $57.61°$. The detector layout of the HMPID is based on a ring imaging Cherenkov detector and is designed to identify particles with $p_T > 1\,\text{GeV}/c$ [C+04].

At the bottom of ALICE, the PHOton Spectrometer (PHOS) is placed at $|\eta| < 0.12$ with a azimuthal coverage of $100°$. It is a high-resolution electromagnetic spectrometer which was built to detect electromagnetic particles and photons. The requirements of the PHOS are a good photon identification with a high energy and spatial resolution [C+04]. On the opposite azimuthal site of the experiment, the ElectroMagnetic Calorimeter (EMCal) is positioned at $|\eta| < 0.7$ with an azimuthal coverage of $120°$. Like the PHOS, the calorimeter is designed to detect photons in ALICE. The φ coverage nearly opposite of the PHOS has been chosen to allow photon-jet measurements in coincidence with the PHOS. In addition, the EMCal improves the enhancement of high p_T events with its high p_T photon trigger [Ron09].

The forward muon spectrometer is placed at $-4.0 \leq \eta \leq -2.5$ and measures $\mu^+\mu^-$ with $p_T > 4.0\,\text{GeV}/c$. The muon spectrometer has to be shielded from the hadrons and photons which are created in the collisions. Only Lorentz boosted muons with $p_T > 4.0\,\text{GeV}/c$ fly through the used absorber, which mainly consists of carbon and concrete. Therefore, the spectrometer is located at this high pseudo-rapidity. One main aim of the muon spectrometer is to measure the $\mu^+\mu^-$-spectrum to reconstruct the heavy quark states like the quarkonia [C+04].

Further detectors are the forward detectors V0, T0 and the Forward Multiplicity Detector (FMD). The V0 detector produces trigger signals and gives a centrality measure. In addition to this, the V0 is a control of the luminosity of the LHC. The T0 is designed to measure the real time of the collision with a precision better than $50\,\text{ps}$. It provides the reference signal for the TOF. In addition, the T0 measures the

vertex position of the collision and selects these within the accepted values. Vertex positions outside this region are identified as beam-gas interactions and rejected. The FMD measures the charged particle multiplicity in the range $-3.4 \leq \eta \leq -1.7$ and $1.7 \leq \eta \leq 5.1$ in full azimuth [C$^+$04].

4. HBOM Simulations

In this chapter, simulations of the HBOM method are described. This method can correct the detector effects without knowing the correlations in the event. First the configuration, which was identified as the best one, is introduced. Then it is compared to slightly different applications of the HBOM method. Of course major modifications are possible, but they lead to worse results.

In Section 4.1, the simulation of a Pb-Pb collision and the application of detector effects are described. After this, different detector hit and fitting methods are discussed. This means that different methods of doing the HBOM analysis are presented and compared.

On the basis of all this methods, the systematic uncertainty is discussed in Section 4.5. There the dependence on the used number of detector hits is also discussed. Besides the standard deviation, higher moments can also be corrected for detector effects, which is described in Section 4.6. At last, two possibilities to correct the whole δp_T distribution are discussed.

4.1. Event Simulation

The events are simulated by the simulation "mypythiaPbPb.cc". The multiple application of the detector effects have been added to the basic program, which was developed by [KB11].

First, the multiplicity of each event is randomly chosen from the multiplicity spectrum for $0 - 10\,\%$ centrality shown in Figure 4.1. In this master thesis, only this centrality is used. Then this number of particles is simulated. For this, each particle gets a random η between -0.9 and 0.9 and a random φ considering flow. This is described in more detail later in this section. The last property of the particle is the transverse momentum p_T, which is randomly chosen following the measured p_T shown in Figure 4.2. This p_T spectrum shows the probability of producing a particle with a certain p_T and is obtained from the 2010 Pb-Pb data (in ALICE terminology the run period LHC10h). The used spectrum goes up to $p_T = 150\,\mathrm{GeV}/c$, but is only shown up to $20\,\mathrm{GeV}/c$ because most of the simulated particles originate from this range. Each event consists of up to 2800 particles (cf. Figure 4.1) which have a p_T following this p_T spectrum. Even in more than 100 events only a very small number of particles will be generated with $p_T > 20\,\mathrm{GeV}/c$.

All simulations are done with the 2010 multiplicity and p_T spectrum. For 2011, the spectra are the same, and therefore, there is no need to do extra simulations with them. In the appendix C, the comparison of the 2010 and 2011 spectra is displayed.
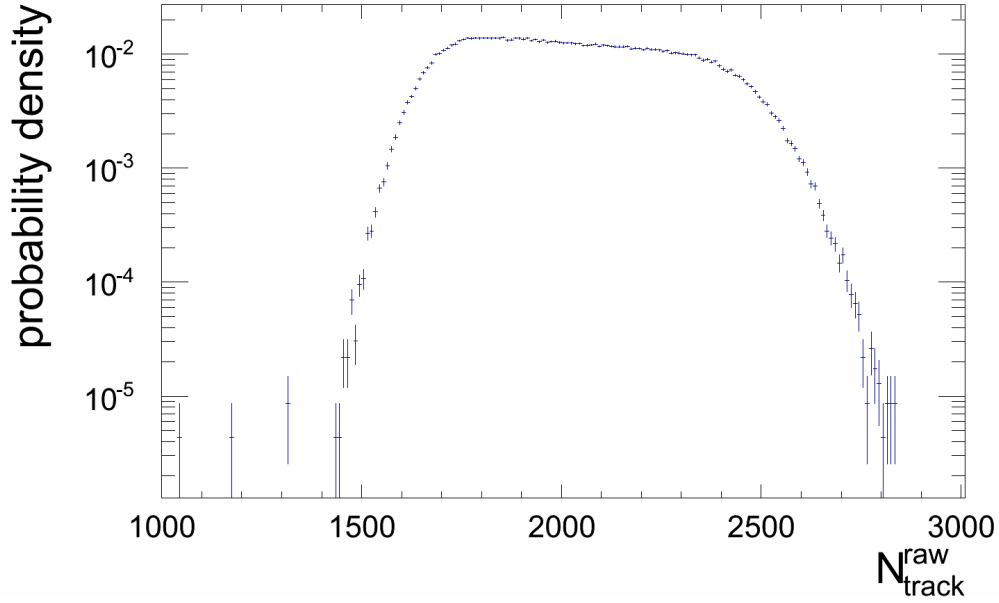
Figure 4.1.: Multiplicity spectrum for $0-10\%$ centrality calculated from 2010 Pb-Pb data (LHC10h). The multiplicity of each simulated event is randomly chosen from this multiplicity distribution. This spectrum is based on the data available online at [KBa]. The used runs are displayed in Appendix B.

The φ value is randomly chosen per particle, taking into account the modulation of the φ distribution due to flow. Equation 4.1 shows the φ dependence of the particle spectrum up to third order of the flow parameter ν

$$\frac{\mathrm{d}^2 N}{\mathrm{d}\varphi \mathrm{d}p_T} = N_0(1 + 2\nu_1(p_T) \cdot \cos\varphi + 2\nu_2(p_T) \cdot \cos\{2(\varphi - \psi_2)\}$$
$$+ 2\nu_3(p_T) \cdot \cos\{3(\varphi - \psi_3)\}). \qquad (4.1)$$

To guarantee the correct φ dependence, this angle is randomly chosen for all particles from the formula in Equation 4.2 which contains all φ dependencies of the last equation

$$f(\varphi) = 1 + 2\nu_1(p_T) \cdot \cos\varphi + 2\nu_2(p_T) \cdot \cos\{2(\varphi - \psi_2)\} + 2\nu_3(p_T) \cdot \cos\{3(\varphi - \psi_3)\}. \quad (4.2)$$

At mid-rapidity, there is no directed flow and thereby $\nu_1 = 0$. The symmetry planes for elliptic and triangular flow ψ_2 and ψ_3 are independent from each other and randomly chosen for every event. The elliptic and triangular flow parameters ν_2 and ν_3 are linearly extrapolated between 0 and $2\,\mathrm{GeV}/c$. For particles above $2\,\mathrm{GeV}/c$, the flow for particles at $2\,\mathrm{GeV}/c$ is used. The used flow values are taken from [A$^+$11] for $0-5\,\%$ and from [A$^+$12a] for $5-10\,\%$ centrality. In the simulation, only the average of these flow values without weighting with the different particle yield of the centrality bins is used. In Table 4.1, the flow parameters at $2\,\mathrm{GeV}/c$ are shown. An example of the
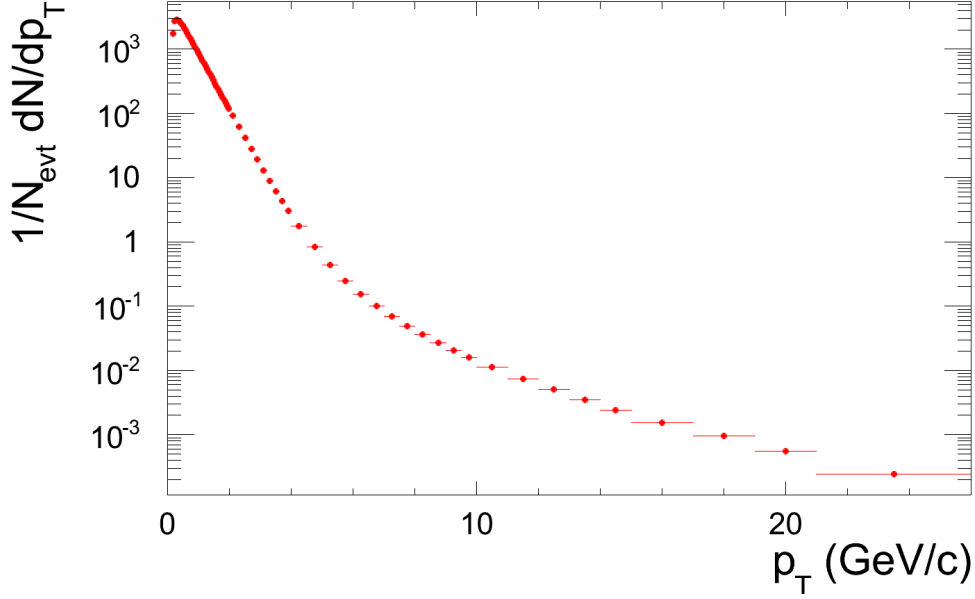
Figure 4.2.: p_T dependent particle spectrum for $0 - 10\%$ centrality obtained from 2010 Pb-Pb data (LHC10h). The spectrum goes up to a transverse momentum of $150\,\text{GeV}/c$, but the probability of having a particle with more than $20\,\text{GeV}/c$ in an event with up to 2800 particles is very small. This spectrum is based on the data available online at [KBa]. The used runs are displayed in Appendix B.

variable	value
ν_1	0
ν_2	0.08
ν_3	0.07

Table 4.1.: Values of the flow parameters at $2\,\text{GeV}/c$. The shown values are averaged over the centrality bins $0 - 5\,\%$ [A$^+$11] and $5 - 10\,\%$ [A$^+$12a] without weighting with the different particle yield. Between 0 and $2\,\text{GeV}/c$ the flow is linearly extrapolated. Above $2\,\text{GeV}/c$, the flow parameters at $2\,\text{GeV}/c$ are used.
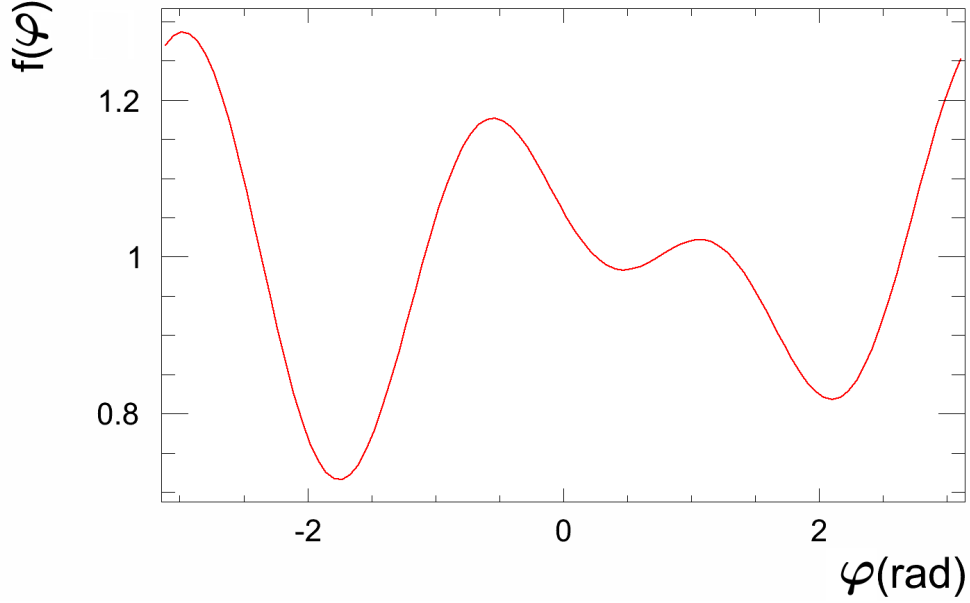
Figure 4.3.: Example function for the elliptic and triangular flow which describes the flow for a $2\,\mathrm{GeV}/c$ particle bin in one event. The symmetry plane of the elliptic flow is set to $\psi_2 = 0$ and of the triangular flow to $\psi_3 = 1.3$.

function $f(\varphi)$ is also shown in Figure 4.3 with a v_2 symmetry plane of $\psi_2 = 0$ and v_3 symmetry plane of $\psi_3 = 1.3$. This is one example of a possible flow symmetry plane configuration. Each event will have a different configuration of the flow symmetry planes $\psi_{2,3}$.

In the simulation, all particles are randomly placed in the events. Therefore, there are no jet correlations in the events. However, the p_T distribution of all particles and the multiplicity is the same as in real events.

In Figure 2.7, the δp_T distribution is already shown as determined from $1.6 \cdot 10^6$ events. It is interpreted as the "true" spectrum. In the following section, the spectra will be normalized to 1 to get a probability density.

Now the detector effects have to be considered to get the measured spectrum. This is done for each particle individually by comparing a random number with the corresponding detection efficiency (cf. Section 2.6). After this procedure, which is called a "detector hit" in this thesis, the δp_T spectrum is determined again.

To correct this detector effects, the HBOM method is used. Again a detector hit is executed and a δp_T spectrum is determined. This is done up to five times. Figure 4.4 shows the determined δp_T distributions for each number of detector hits. Attention should be paid to the fact that zero detector hits are the measured data and not the "true" spectrum.

Any observable of interest can be determined out of the δp_T distributions and then back-extrapolated to a detector effect of zero. The simulated δp_T distribution without
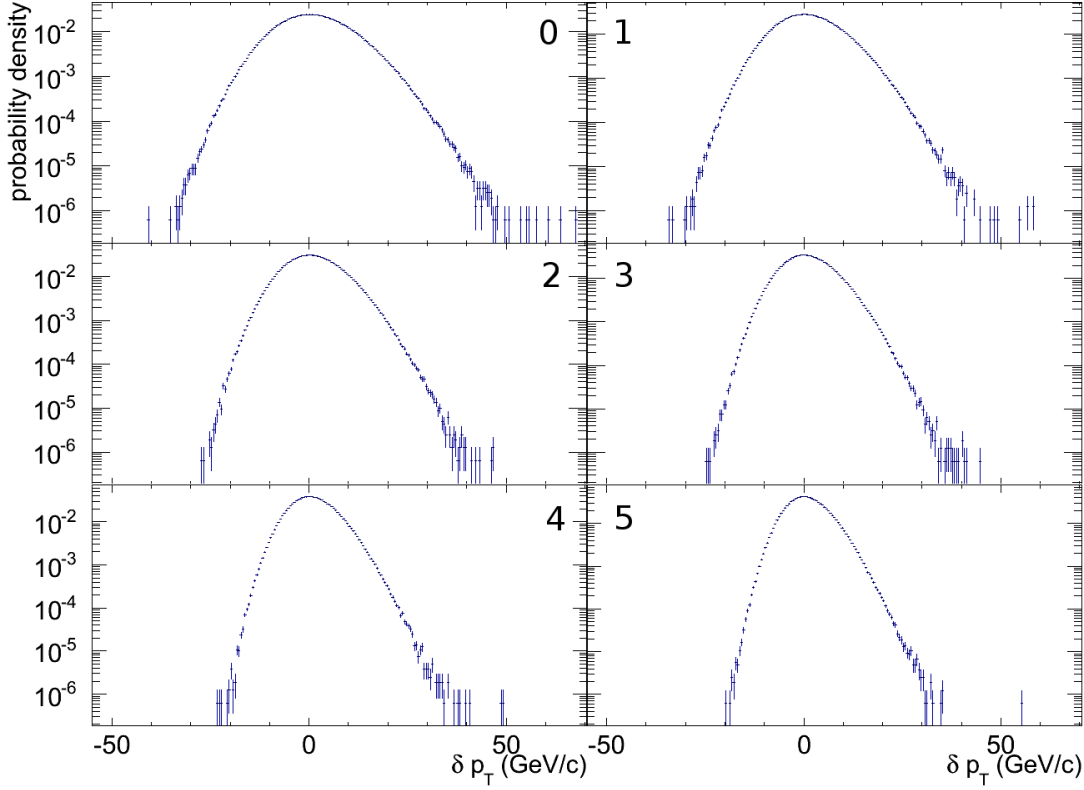
Figure 4.4.: δp_T distribution depending on the detector hits. From top left to bottom right $0-5$ detector hits. These distributions are made of $1.6 \cdot 10^6$ simulated events. The spectrum with zero detector hits is the measured spectrum and is not the same as in Figure 2.7. Compared to the "simulated" spectrum the measured spectrum has one detector hit more.

any detector effects (= the "true" spectrum) gives a comparative value to evaluate the quality of the back-extrapolation. Here $\sigma(\delta p_T)$ is the chosen observable, which is plotted against the detector hits in Figure 4.5.

The measured value for 0 detector hits is $\sigma = (8.330 \pm 0.005)\,\mathrm{GeV}/c$. From Figure 2.8 a value between 8.0 and $10.0\,\mathrm{GeV}/c$ for 2000 tracks can be expected. While the lower value is from random cones in real events with randomized tracks, the upper one is from random cones in real events. The simulation described in this chapter uses randomized tracks following a real track p_T. Beside this, all particles following a p_T dependent flow formula. Thus, the differences are the additional consideration of the flow for the lower reference value and the usage of randomized tracks for the upper reference value. The result of the measured standard deviation $\sigma = (8.330 \pm 0.005)\,\mathrm{GeV}/c$ is within the expected range.

The aim of the HBOM method is to get the "true" value (-1 detector hits) from all other points. For this purpose, the other points are fitted, and then the fit function is back-extrapolated to -1 detector hits. Different possible fit functions are described in the next section.
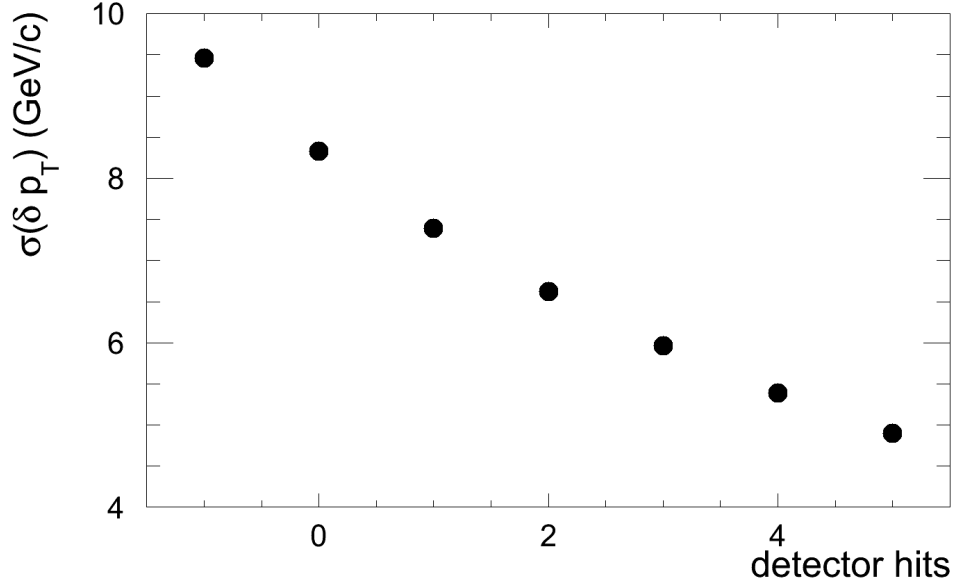
Figure 4.5.: HBOM method for $\sigma(\delta p_T)$ up to five detector hits. -1 detector hits show the $\sigma(\delta p_T)$ of the simulated (= "true") distribution in Figure 2.7. In Figure 4.4, the distributions for the other corresponding detector hits are shown. The point at zero detector hits corresponds to the measured spectrum.

4.2. Fit Function for the Back-Extrapolation

In Section 2.6, the back-extrapolation of an observable has already been explained and shown (cf. Figure 2.11). The back-extrapolation was done with a polynomial fit of third order with parameters a,b,c,d

$$f(x) = ax^3 + bx^2 + cx + d. \tag{4.3}$$

A polynomial function is quite flexible in the fitting process. For the points in Figure 4.5, the fitting with a polynomial function works well, but it must be checked if there is an extremum (maximum or minimum) or an inflection point between the last fitting point and the extrapolated point. If there is one, the extrapolation fails. Usually it is no problem to extrapolate to -1 detector hits for the observable $\sigma(\delta p_T)$. It was found that it is often not possible to extrapolate in the direction of more detector hits. So the point at five detector hits is not suitable as a quality check.

Another possible functional form suggested by the data is an exponential function. An empirical well working fit function is presented in Equation 4.4 and used to fit the points in Figure 4.5

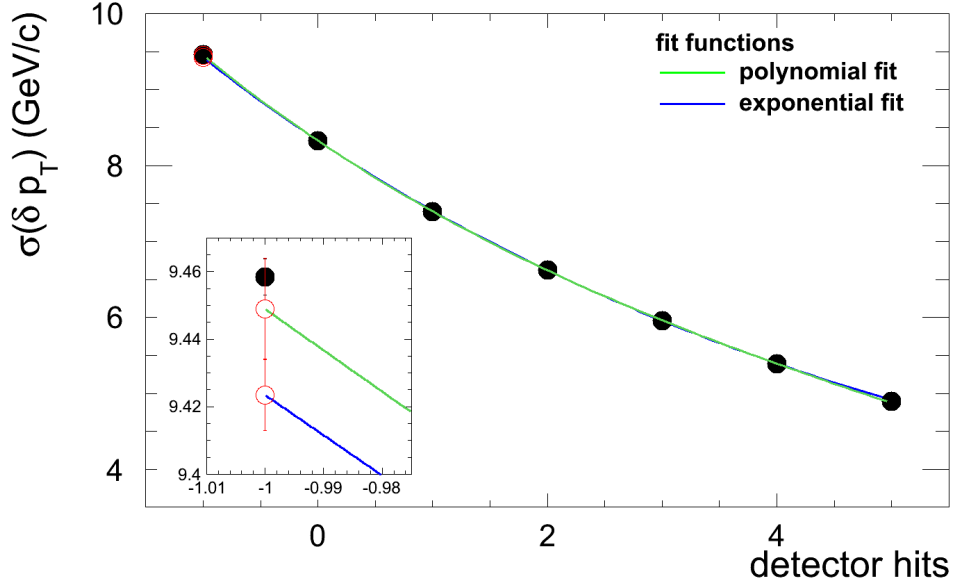$$f(x) = a \cdot e^{-bx^2 - cx} + d. \tag{4.4}$$

Figure 4.6.: HBOM method for $\sigma(\delta p_T)$ up to five detector hits. A polynomial function of 3rd order (green, Equation 4.3) and an exponential function (blue, Equation 4.4) is fitted to the points zero to four. The open red circles indicate the back-extrapolated points of the fit functions. In the zoomed view, it can be seen that the polynomial back-extrapolation agrees better with the simulated point (black) than the exponential back-extrapolation. The simulation contains $1.6 \cdot 10^6$ events.

This function has also four free parameters and defines a certain shape of the fit function. The extremum at $x_{min} = -\frac{c}{2b} = 28$ is behind the 5th detector hit and not within the observed range. Therefore, the extrapolation to -1 detector hits works for sure. Also the extrapolation in direction of more detector hits works because there is no extremum between four and five detector hits. So the fifth detector hit is a possible quality check for the fit which does not need the knowledge of the "true" data point. This fit can only be used for data points which follow this functional shape. For example, higher moments like the skewness can have a completely different functional behavior (cf. Section 4.6). Here, the polynomial or another fit function must be used. To decide which function to use in the further implementation, an HBOM simulation was done and both fits were used to back-extrapolate the $\sigma(\delta p_T)$. The statistical uncertainties of the back-extrapolation are determined out of the covariance matrix of the fit. Figure 4.6 shows the fitted curves.

Both curves agree with each other, and the error bars of the back-extrapolated points overlap. In the zoom can be seen that the polynomial back-extrapolation agrees with the simulated point within its error bar. The one from the exponential function also provides a good approximation, but it does not overlap with the error bar of the

simulated point.

One value which describes the quality of a fit is the χ^2/NDF. It describes the deviation of the points from the fit divided by the degrees of freedom (NDF) of the points. The NDF are calculated by subtracting the degrees of freedom of the fit (always four in this thesis) from the degrees of freedom of the points (mostly five, because of five points used for the fit). In almost every case the result is $NDF = 1$. The values of the back-extrapolated points and the χ^2/NDF are also shown in Table 4.2.

fit	corrected point	χ^2/NDF
simulation	9.458 ± 0.005	
polynomial	9.449 ± 0.020	2.2
exponential	9.423 ± 0.011	6.0

Table 4.2.: Position of the back-extrapolated points with different fit functions.

The χ^2/NDF for the polynomial fit is much better than the one for the exponential fit. A good value is between one and two. Compared with the simulation also the polynomial fit provides the better result. Hence the polynomial back-extrapolation will be used as the standard method. The exponential fit will be considered to estimate the systematic uncertainty of the back-extrapolated point.

4.3. Detector Position

In this section, the effect of a rotating detector compared to a fixed detector is discussed. A fixed detector means that the efficiency to detect a particle at a given φ and p_T is constant for all detector hits, while a rotating detector means that the detector is rotated in φ after each detector hit. This is optimized so that the efficiency holes of the detector (cf. Figure 2.10) are uniformly distributed over the event. Due to the segmentation of the TPC, there are 18 efficiency holes in each event. After each detector hit, the detector is rotated about $360°/(18 \times N)$, where N is the overall number of detector hits. This means e.g. for overall two detector hits the detector is rotated by $10°$ after the first detector hit. For e.g. five detector hits the detector is rotated by $4°$ after each of the first four detector hits. The fixed detector will be called the normal detector as it is equal to the simulation in Section 4.2 with the polynomial fit.

In the case of the normal detector there are almost no particles left at the position of a detector hole after a few detector hits. This is avoided by the rotating detector. After each detector hit, the detector is rotated so that the efficiency holes lie on positions where a high tracking efficiency was to be found in the detector hits before. A consequence of the rotating detector is the higher number of removed tracks. The particle deficient areas at the efficiency holes for the normal detector are the reason for this. In the later detector hits, there are rarely particles left which can be removed from the event. However, there are always many particles which can be removed in the rotating detector. This is due to the fact that the efficiency holes change their position
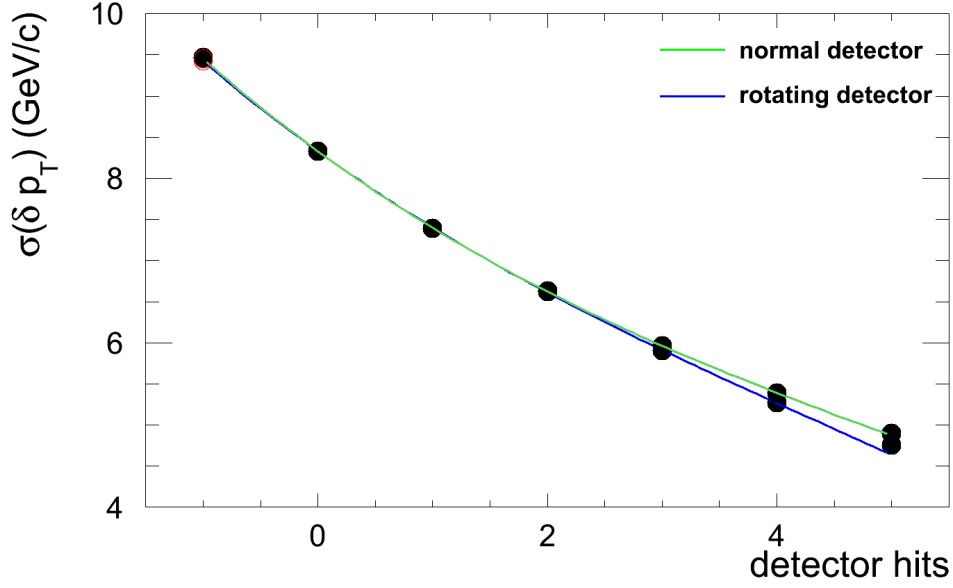
Figure 4.7.: Comparison between the normal (fixed) and rotating detector. The open red circles show the back-extrapolated values. They are also shown in Figure 4.8 for a better comparison.

in the detector after each detector hit.

Both models have been simulated, and the results are shown in Figure 4.7. $\sigma(\delta p_T)$ is smaller in the rotating detector than in the normal detector for detector hits > 1. By rotating the detector, the efficiency to detect particles in every area of an event becomes homogeneous for high detector hits. In section 2.4, the determination of the δp_T spectrum is explained. A random cone with radius $R = 0.4$ is placed randomly in the event. For the normal detector (or only 1 detector hit in the rotating detector), the distance between two efficiency holes is $d = 2\pi/18 = 0.35$. Every random cone will hit at least two efficiency holes. However, it makes a big difference if a cone is located central over an efficiency hole or if it only touches it peripheral.

After a few detector hits, the distance between two efficiency holes gets smaller for the rotating detector. Furthermore, the particle density in all these holes is much higher than the particle density in an efficiency hole of the normal detector because only one real efficiency hole hits these φ areas. The highest and lowest δp_T values in the normal detector simulation do not originate only from regions of high and low transverse momentum. On top of this, the random cone covers the least space or the most space of an efficiency hole to produce extreme values of δp_T. In the rotating detector, hardly any different coverage is possible. For example, for five detector hits the distance of two detector holes is $d = 2\pi/(18 \cdot 5) \approx 0.07$. So the random cones covers five or six efficiency holes. There is not much difference in the covered efficiency-hole-area possible, which leads to a suppression of extreme values in the δp_T distribution of the
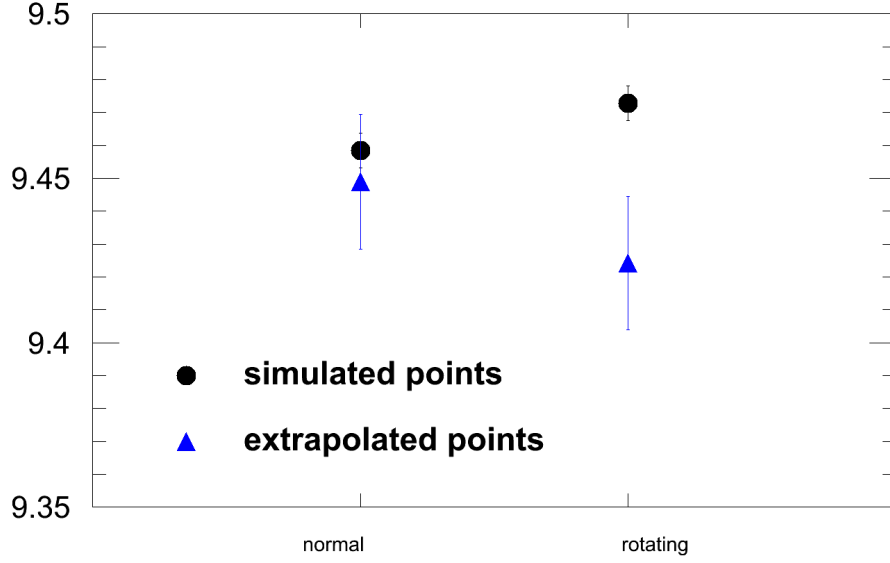
Figure 4.8.: Comparison of the back-extrapolated $\sigma(\delta p_T)$ values for the normal $((9.449 \pm 0.020)\,\text{GeV}/c)$ and rotating detector $((9.424 \pm 0.020)\,\text{GeV}/c)$. The difference of the simulated points of the two models is caused by statistical fluctuations.

rotating detector. This is the major reason why the $\sigma(\delta p_T)$ is lower for the rotating detector at high detector hits.

The other reason is the lower multiplicity in the events. Because the low efficiency is always applied on areas with high multiplicity in the rotating detector, more particles are rejected than in the normal detector. With lower multiplicity, the standard deviation of the δp_T distribution also goes down.

Which method gives the better back-extrapolation has to be determined by the comparison with the simulated value. This comparison in Figure 4.8 shows that the normal detector provides a better approximation to the "true" value. In conclusion, the normal detector was used in further analysis.

4.4. Dependent and Independent Detector Hits

The detector hits can be calculated in two different ways (cf. Section 2.6). Either every detector hit i is calculated after its previous detector hit, and the remaining particles are used as input spectrum for the next detector hit (dependent), or all detector hits are calculated at the same time, and the efficiency to detect it i times is considered for each particle (independent). Here the independent simulation, which uses the independent detector hits, is identical to the simulation in Section 4.2 and the normal detector in Section 4.3.
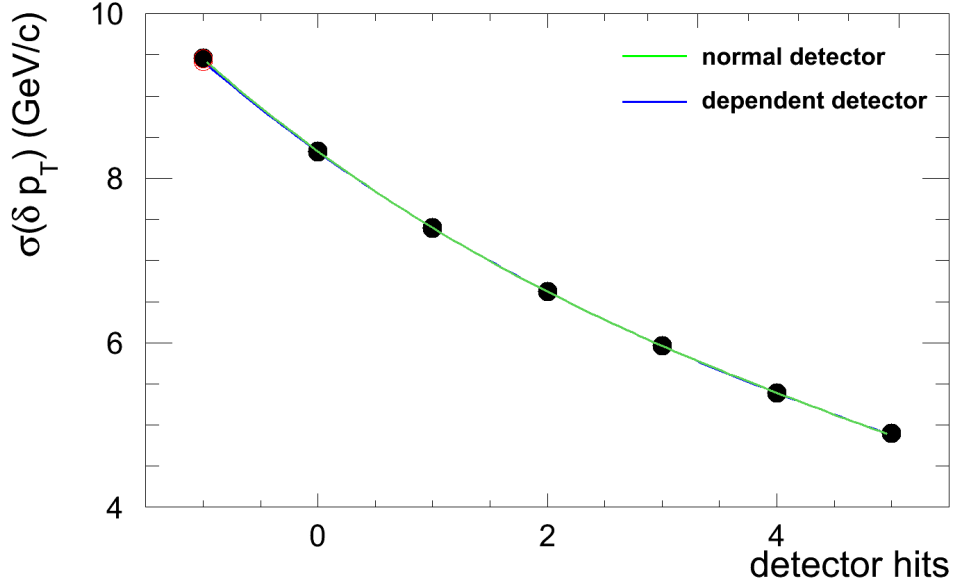
Figure 4.9.: Comparison of independent and dependent detector hits. The extrapolated values of both simulations are also shown in Figure 4.10.

The difference of the dependent and independent detector hits is the efficiency which is used to test if the particles are detected or not. In the dependent detector hit, the probability p of detecting a particle is the detector efficiency ϵ

$$p = \epsilon.$$

The output of the previous detector hit is used as the input spectrum. For the independent detector hit, the detector efficiency has to be considered i times. So the probability that the particle remains in the event is

$$p = \epsilon^i.$$

Here the input spectrum is always the measured spectrum. A particle which is removed in the first detector hit cannot appear after the next detector hit for the dependent simulation. In the independent simulation, this particle could be included in the event after two detector hits although it is not included in the event after one detector hit. One advantage of the independent approach is an easier method of parallelizing the algorithm. Besides this, an extra detector hit could be easier done after the simulation was already finished. Using the dependent simulation, all events have to be stored to calculate an extra detector hit or the whole simulation has to be repeated.

Both models have been tested, and the results are presented in Figure 4.9. Obviously the differences are small between these two approaches. The resulting $\sigma(\delta p_T)$ are almost equal, and the fits are nearly the same. In Figure 4.10, the back-extrapolation
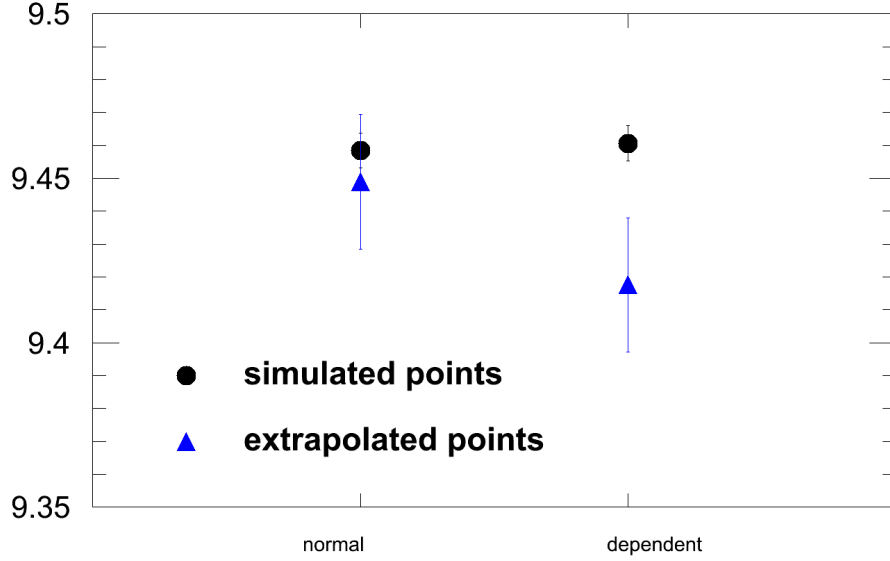
Figure 4.10.: Comparison of the back-extrapolated $\sigma(\delta p_T)$ values for independent (= normal detector: $(9.449 \pm 0.020)\,\text{GeV}/c$) and dependent $((9.418 \pm 0.020)\,\text{GeV}/c)$ detector hits. The difference of the simulated points of the two models are caused by statistical fluctuations.

of both methods are plotted together with their "true" (simulated) value of $\sigma(\delta p_T)$. Within the error bars, the dependent and independent simulation provide the same result. Nevertheless, the independent simulation is the better approximation to the simulated points. In conclusion, the normal simulation is used in the following sections.

4.5. Systematic Uncertainty

The systematic uncertainty of the HBOM analysis is made up of the different approaches explained in the last sections and the number of points used in the back-extrapolation. Figure 4.11 shows the difference in using 0...4, 0...5 or 0...6 points in the back-extrapolation. Attention should be paid to the fact that five used points correspond to a maximum used detector hit of four. The values of the extrapolated points are shown in Table 4.3. It can be seen that the back-extrapolation gets worse with more points. To use only four points for the back-extrapolation does not provide better results because the fitting function contains four parameters. Of course it is always possible to fit four points with this function. However the extrapolation cannot be trusted outside the fitted points.

For the calculation of the systematic uncertainty, the deviation between the respective methods is calculated. For the different number of fit points, the deviation $|\sigma_5 - \sigma_6| = |9.449\,\text{GeV}/c - 9.427\,\text{GeV}/c| = 0.022\,\text{GeV}/c$ is used. In Table 4.4, this
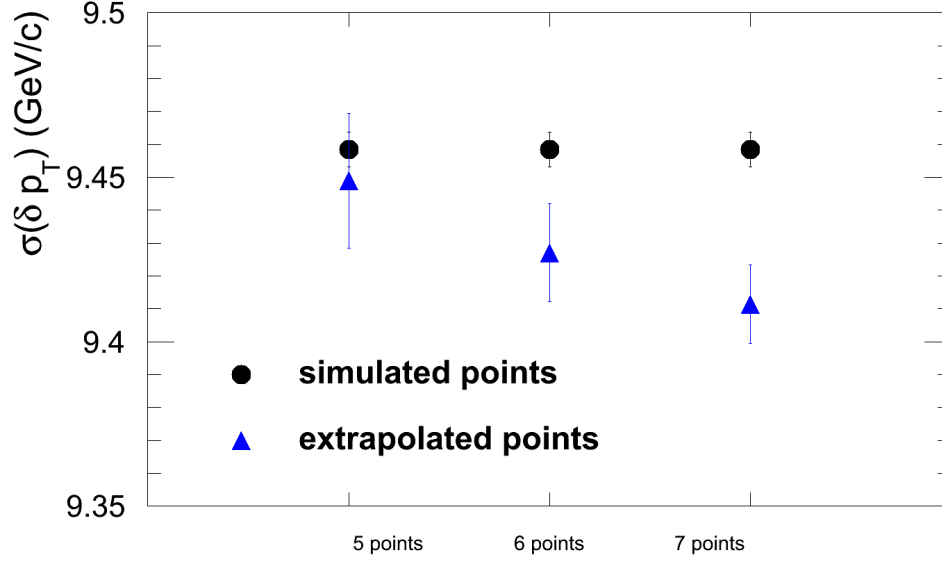
Figure 4.11.: Back-extrapolation for different number of used points in the fit.

points	corrected point	χ^2/NDF
0	9.458 ± 0.005	
5	9.449 ± 0.020	2.2
6	9.427 ± 0.015	2.3
7	9.411 ± 0.012	2.6

Table 4.3.: Position of the back-extrapolated points with different number of fitting points. In the first line with zero points, the simulated value is displayed.

and the deviations between the different models of the last sections are shown. All
back-extrapolations are summarized in the appendix in Table F.1.

method	deviation [GeV/c]
fit points	0.022
fit function	0.026
rotating	0.025
dependent	0.031
$\Delta_{\mathrm{syst}}^{sim}\sigma(\delta p_T)$	0.052

Table 4.4.: Deviation between the back-extrapolated points for different approaches.
The comparative value in each method is the same "normal" value.

The systematic uncertainty for the whole HBOM method is calculated as the squared
sum of all deviations. As a result, $\Delta_{\mathrm{syst}}^{sim}\sigma(\delta p_T) = 0.05\,\mathrm{GeV}/c$ is calculated.
Altogether this leads for the standard deviation of the δp_T distribution to a value of
$\sigma(\delta p_T) = (9.45 \pm 0.02(\mathrm{stat}) \pm 0.05(\mathrm{syst}))\,\mathrm{GeV}/c$.

4.6. Higher Moments

One possibility to get more information about the "true" δp_T distribution is to back-
extrapolate the higher moments in addition to the $\sigma(\delta p_T)$ which is the second moment.
For the back-extrapolation of the higher moments, polynomial fit functions are used.
The used higher moments are the skewness γ_1 and the excess kurtosis γ_2:

$$\gamma_1 = \mathrm{E}\left[\left(\frac{X - \mu}{\sigma}\right)^3\right] \tag{4.5}$$

$$\gamma_2 = \mathrm{E}\left[\left(\frac{X - \mu}{\sigma}\right)^4\right] - 3. \tag{4.6}$$

Here E is the expectation operator, μ the mean and σ the standard deviation of the
δp_T distribution. The skewness is a way of measuring the asymmetry of a distribution.
A positive skewness $\gamma_1 > 0$ means a bigger right tail, while most of the points are on
the left side of the distribution. Analog $\gamma_1 < 0$ means a longer left tail, while most of
the points are on the right side.
The excess kurtosis is defined relatively to the kurtosis of the normal distribution,
which is three. Thus the kurtosis is defined like the excess kurtosis without the minus
three at the end. Because of the always positive values of the kurtosis, the extension
to the excess kurtosis is done. A positive $\gamma_2 > 0$ means a sharper peak as the normal
distribution, while a negative $\gamma_2 < 0$ means a flatter peak.
The skewness of the δp_T distribution was determined for all detector hits. In Figure 4.12,
the back-extrapolation is shown with six used points. For the skewness the back-
extrapolation with five points provides bad results. It had an inflection point near
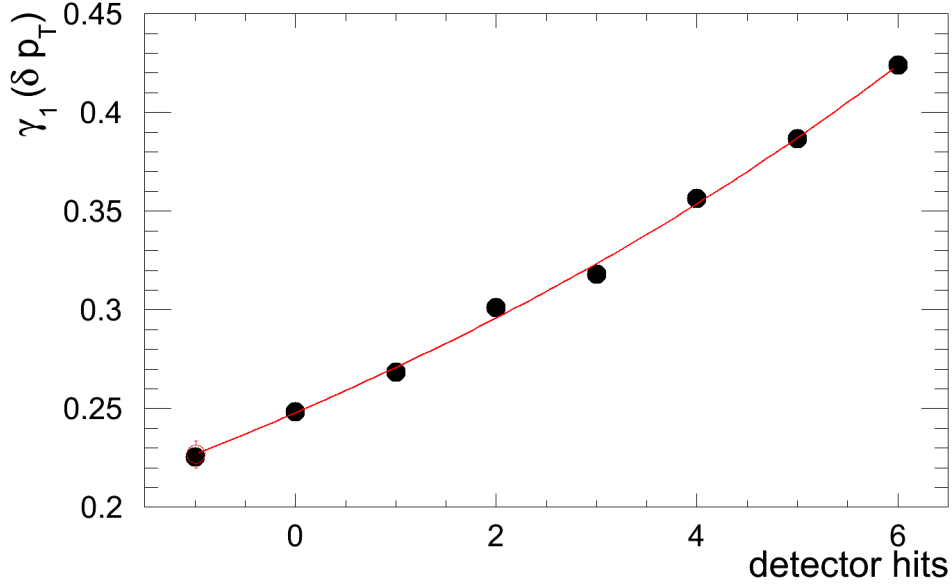two detector hits and underestimated the "true" skewness. Because of the positive

Figure 4.12.: Skewness of δp_T distribution. The measured skewness of $\gamma_1 = 0.248\pm0.002$ is corrected to $\gamma_1 = 0.227 \pm 0.007$. In the simulation $\gamma_1 = 0.225 \pm 0.002$ was determined. For the back-extrapolation, up to five detector hits are used.

tail of the input p_T distribution, the δp_T distribution is a right-skewed one. While the standard deviation σ drops, the asymmetry almost stays constant. As a consequence, the skewness rises.

Figure 4.13 shows the kurtosis of the δp_T distribution. The back-extrapolation was not possible in the usual way. At two and four detector hits the kurtosis is much higher than the kurtosis for one detector hit more. This upward fluctuation is not jet understood. To provide a back-extrapolation the fit is done for zero, one, three, five and six detector hits. These again are five fitting points, which is the usually used number. With these points, the back-extrapolation provides a very good result. The simulated point and the corrected kurtosis are identical.

Additionally, it was found that the fluctuations of the kurtosis is very sensitive to the used simulation method. If the dependent simulation (cf. Section 4.4) is used, the fluctuation does not start before six detector hits. Then a back-extrapolation is possible in the usual way. This is shown in Figure 4.14. The differences between the simulated and measured points for the normal (Figure 4.13) and dependent (Figure 4.14) detector hits are purely statistical fluctuations.

If all points of the kurtosis are on a continuous curve, the back-extrapolation provides very good results. The reason of the fluctuations must be investigated further.
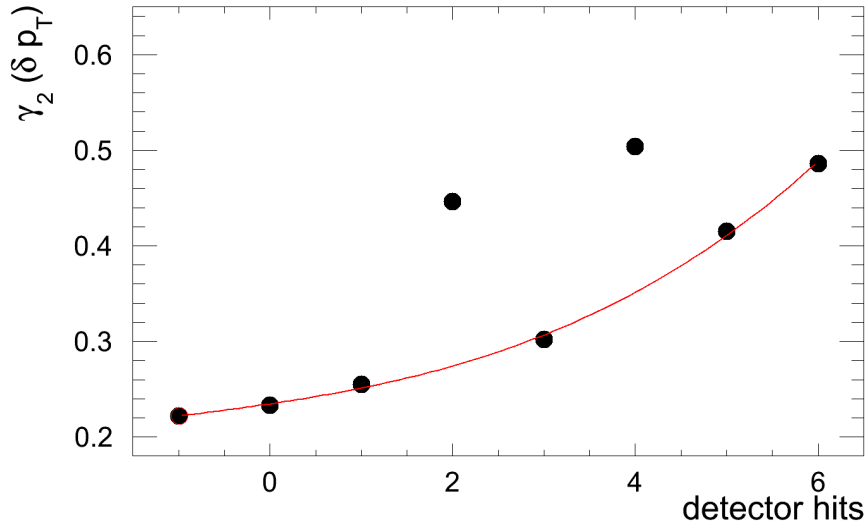
Figure 4.13.: Kurtosis of δp_T distribution. Up to now the jumps at two and four detector hits are not understood and are not used for the fit. The measured kurtosis of $\gamma_2 = 0.233 \pm 0.004$ is corrected to $\gamma_2 = 0.222 \pm 0.004$. In the simulation $\gamma_2 = 0.222 \pm 0.004$ was determined.
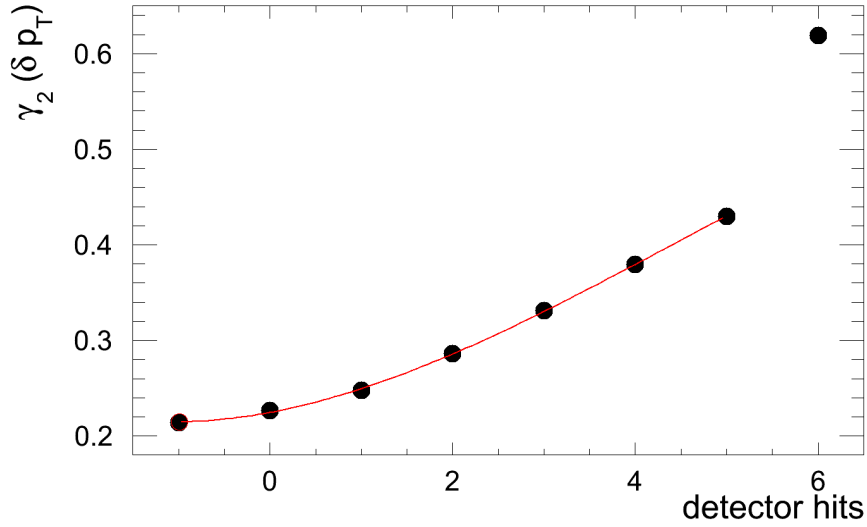

Figure 4.14.: Kurtosis of δp_T distribution. This data is from the dependent simulation (cf. Section 4.4). The result of the first five detector hits seem to have a consistent detector hit dependence, while the sixth detector hit shows a jump. For the fit, only up to four detector hits are used. The measured $\gamma_2 = 0.226 \pm 0.004$ is corrected to $\gamma_2 = 0.215 \pm 0.004$. Simulated was $\gamma_2 = 0.214 \pm 0.004$.
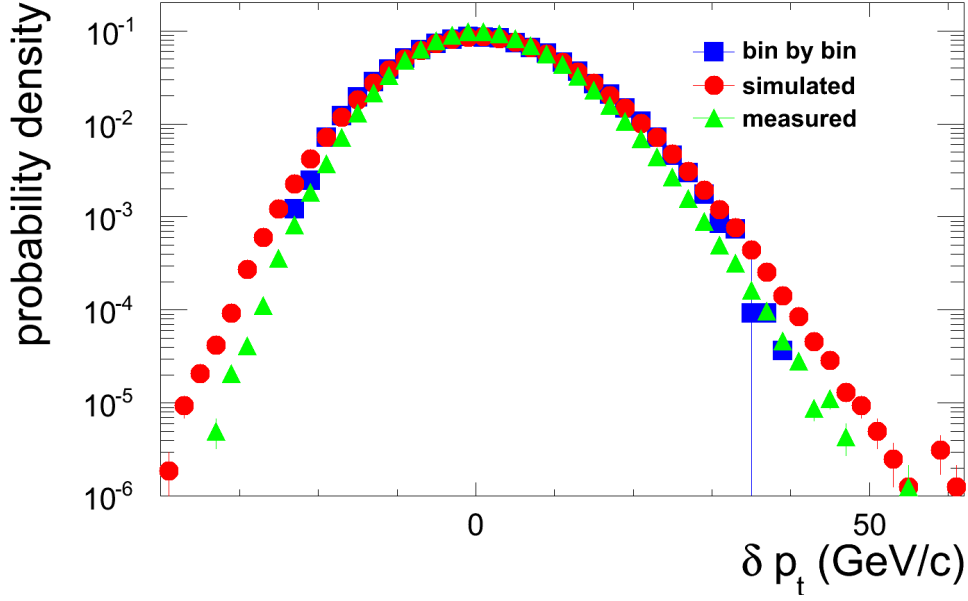
Figure 4.15.: Measured (green) and simulated (red) δp_T distribution. The bin-by-bin (blue) corrected distribution was determined by correcting each bin of the δp_T distribution by the HBOM method. After the correction, the distributions are normalized to an integral of 1.

4.7. Back-Extrapolation of the δp_T Distribution

The determination of higher moments is one possibility to get the whole δp_T distribution corrected. However, the last section showed that it is very difficult to back-extrapolate beyond the third moment of the δp_T distribution. In addition, one still has to build up the whole corrected distribution from those moments. The resulting corrected distribution would have large uncertainties. In this section, two methods are presented which directly correct the whole δp_T distribution and are easier to handle. One possibility is to back-extrapolate each bin on its own. The other one is to take the measured distribution and smear each bin; this way the previous back-extrapolated $\sigma(\delta p_T)$ is reached.

For the first method, each bin of the distribution is handled on its own. The bin content of a bin is determined for all detector hits. Then it is fitted and back-extrapolated to -1 detector hits. In Figure 4.15, the result of this back-extrapolation is shown. To provide an additional reference, the measured δp_T distribution is also shown. The method only works if some of the bin entries n_0 left after all detector hits N

$$\epsilon^N \cdot n_0 > 0 \tag{4.7}$$

If the bin content is empty before the last detector hit, a meaningful fit is no longer possible. An empty bin does not provide any information which could be used, so the
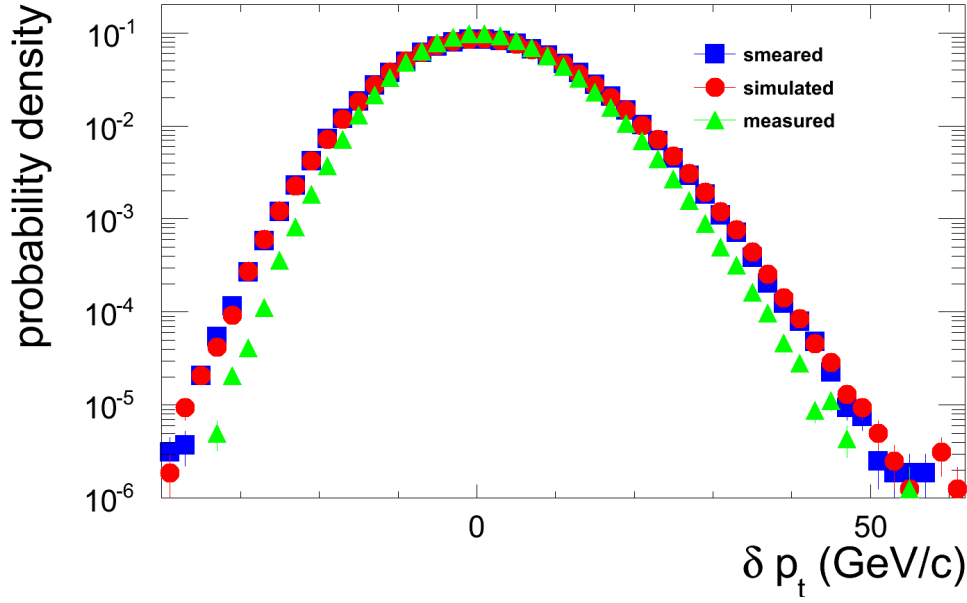
Figure 4.16.: Measured (green) and simulated (red) δp_T distribution. To get the smeared (blue) distribution, the measured one was convoluted with a compressed copy of itself. This procedure was done with a four times finer binning and then rebinned to get better results. After the correction the distributions are normalized to an integral of 1.

quality of the back-extrapolation would drop. Such bin cannot be corrected and is skipped. Therefore, this method reduces the statistical significants of the δp_T distribution.

The quality of the correction is shown in the ratio of the corrected and simulated distribution in Figure 4.17. A line is drawn at an uncertainty of 5%. Between -20 and $+27\,\mathrm{GeV}/c$ the deviation of the corrected distribution from the simulated distribution is one time larger than this 5%, but the results are still acceptable. Outside of this range, there was almost no correction possible, and it provides bad results for the bins where the correction was possible.

The bin-by-bin corrected distribution provides a $\sigma(\delta p_T) = 9.261 \pm 0.025\,\mathrm{GeV}/c$. Compared to the value of the simulation $\sigma(\delta p_T) = 9.458 \pm 0.005\,\mathrm{GeV}/c$ this is a bad result. A better correction of the whole distribution is provided by the smearing method. First, the corrected $\sigma_{HBOM}(\delta p_T)$ is determined with the HBOM method, and then a σ_{smear} is calculated which smears the measured $\sigma_{meas}(\delta p_T)$ to the corrected $\sigma_{HBOM}(\delta p_T)$

$$\sigma_{smear} = \sqrt{\sigma_{HBOM}^2(\delta p_T) - \sigma_{meas}^2(\delta p_T)}. \tag{4.8}$$

Now a copy of the measured distribution is compressed to the standard deviation of σ_{smear}. The aim is to retain the shape of the distribution which includes the jet tail at large positive momenta. Then, the normal measured distribution is convoluted
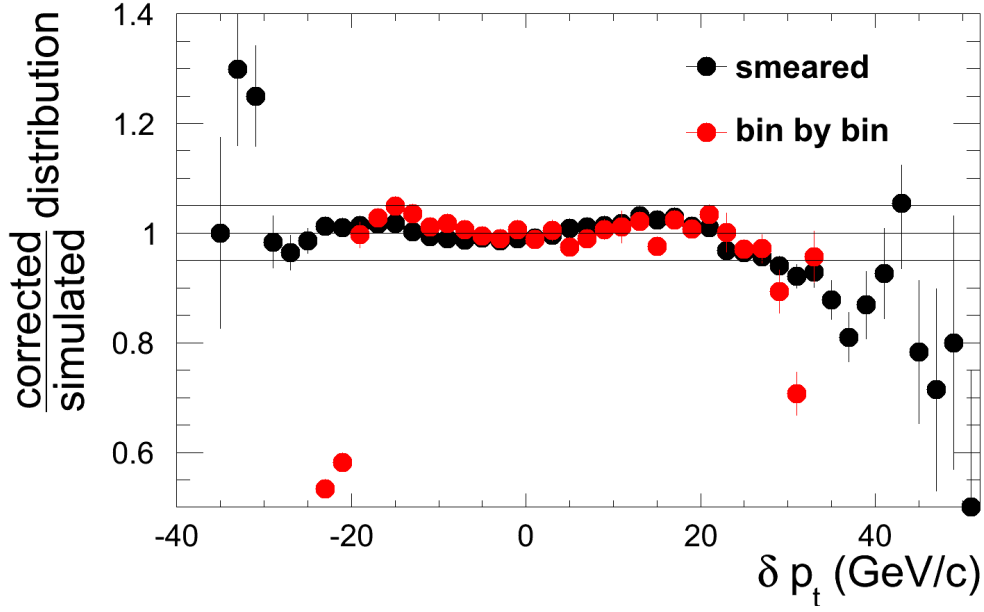
Figure 4.17.: The ratio of the bin-by-bin (smeared) corrected and the simulated δp_T distribution in Figure 4.15 (Figure 4.16) is drawn in red (black). The smeared corrected distribution has a wider range in which it describes the simulated distribution.

with the compressed measured distribution. The result is the smeared distribution in Figure 4.16. In Figure 4.17, the ratio of the smeared and the simulated distribution is shown.

Obviously the smeared distribution provides a wider range in δp_T in which the detector correction could be done. While the smeared distribution provides good results within an error band of $5\,\%$ from -30 to $+27\,\mathrm{GeV}/c$, the bin-by-bin distribution provides this only from -20 to $+27\,\mathrm{GeV}/c$. Outside of the good range, the smeared distribution fluctuates heavily while the bin-by-bin distribution quickly drops to zero. This is also an advantage of the smearing correction because the trend of the distribution is still correct.

Another advantage of the smeared distribution is a possible small binning. To get good results, a binning as small as possible is preferred. The bin-by-bin correction prefers big bins because otherwise the resulting distribution fluctuates very strongly. Additionally, the range in which the back-extrapolation is possible drops further with a finer binning. The advantage of a finer binning is that more information is retained.

Summary

In this chapter, the HBOM method was analyzed for different specifications. The best detector hit method is a fixed detector with independent detector hits. The polynomial fit with five fitting points is chosen as the fitting method. This configuration is used as standard for the data analysis.

The correction of the whole δp_T distribution was shown. Only the smearing method can correct the distribution over a broad p_T range, while the bin-by-bin correction has only a limited range. Also, the bin-by-bin corrected distribution provides a bad standard deviation $\sigma(\delta p_T)$. Here the smeared distribution could not used for a comparison because the resulting standard deviation is per definition equal to the HBOM correction. Altogether, the smearing method is preferred to correct the whole δp_T distribution.

5. HBOM Data Analysis

After the analysis of the HBOM method in simulations, the method is applied to 2010 and 2011 Pb-Pb data in the following sections. In particular, the used run periods are LHC10h and LHC11h. The h stands for a run period in the corresponding year and contains Pb-Pb runs in both years. First, the back-extrapolation of $\sigma(\delta p_T)$ is discussed. Then, the correction of the higher moments and the whole distribution is presented.

5.1. Back-Extrapolation of 2010 Data

The δp_T distribution for the data analysis differs slightly from the one in the simulation because the particle tracks are not randomized. As for the simulation, the two leading jets are excluded for the background calculation. This means the background is calculated after subtracting the two leading clusters. However, random cones can contain parts of these leading jets. This way the δp_T distribution contains region to region fluctuations and jets. Due to these jets, the standard deviation from the data analysis is expected to be higher than from the simulation where randomized tracks were used (cf. Section 4.1).

For the analysis the AliRoot analysis task AliAnalysisTaskJetHBOM[1] was developed; the revision number used for the final results is 58309. As usual for the analysis, the setup is a minimum track $p_{T,min} = 0.15\,\mathrm{GeV}/c$. The analyzed LHC10h data after the detector hits is available online (see [Zima]). All runs used in the analysis are displayed in the appendix in Table B.3.

In Figure 5.1, the back-extrapolation of the LHC10h data is shown. The polynomial fit from zero to four detector hits is used as the fitting method. The measured value of $\sigma(\delta p_T) = (10.165 \pm 0.006)\,\mathrm{GeV}/c$ is corrected to $\sigma(\delta p_T) = (11.817 \pm 0.026)\,\mathrm{GeV}/c$. Compared to the simulated result of $\sigma(\delta p_T) = (9.43 \pm 0.02(\mathrm{stat}) \pm 0.11(\mathrm{syst}))\,\mathrm{GeV}/c$, the experimental values are higher. This is expected because the simulation does not include all effects that are present in the data.

Compared to the expectations from Figure 2.8, the data value is lower. There the measured standard deviation for the background calculation (red circles) can be read to $\sigma(\delta p_T) = (10.8 \pm 0.2)\,\mathrm{GeV}/c$ at $N_{\mathrm{input}}^{\mathrm{raw}} = 2000$, which is the mean number of tracks in the centrality $0 - 10\%$. The analysis in [A$^+$12b], from which the Figure comes, uses old track cuts compared to the analysis in this thesis. Additional the GoldenChi2 cut is used here which compares the χ^2 of the global and the TPC fit. A consequence of

---

[1]The used class is AliAnalysisTaskJetHBOM.cxx with its header AliAnalysisTaskJetHBOM.h and the macro AddTaskJetHBOM.C.
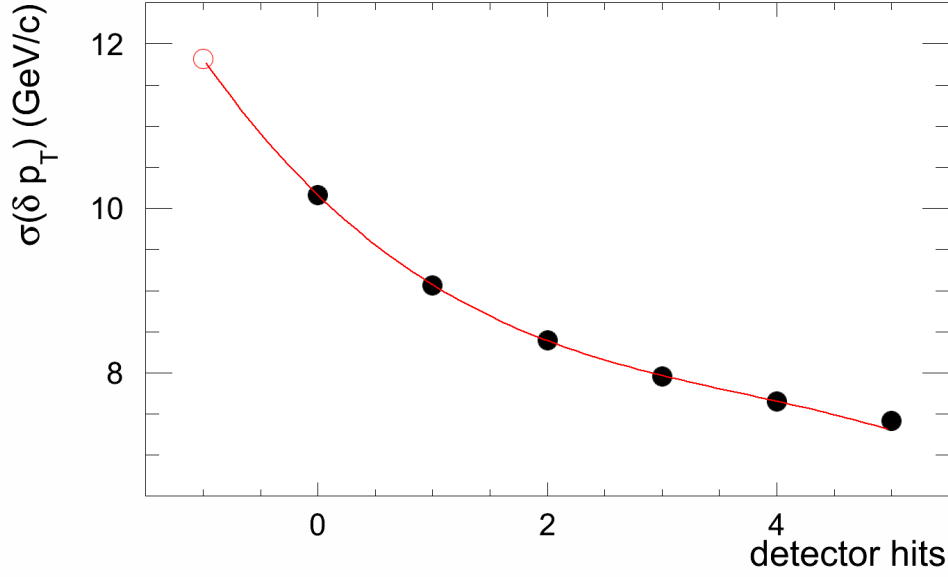
Figure 5.1.: Back-extrapolation of $\sigma(\delta p_T)$ for LHC10h data with $1.6 \cdot 10^6$ events. For the fit, the points from zero to five detector hits are used. The values are described in the text.

this cut is a lower efficiency of around 4%. This leads to a lower multiplicity and a changed p_T spectrum. The cut is mainly used to reject high-p_T outliers. Equation 2.8 shows that the changes lead to a lower standard deviation. This explains the lower standard deviation in the analysis shown here.

Furthermore, the published value is for one multiplicity, while the data value is for a centrality range of $0 - 10\%$. This centrality corresponds to a multiplicity from 1700 to 2500 tracks (cf. Figure 4.1). This means that there is another not dominating uncertainty for the comparison which is not considered.

Obviously the fit does not describe the fifth detector hit. An exponential fit may work better in this context. But in the simulation (cf. Section 4.2), the polynomial fit provided better results, and it is assumed that this is the case for the data analysis, too. It is not important that the fit continues well in the direction of more detector hits. In contrast, the direction towards -1 detector hits is essential. The analysis of the systematic uncertainty in Section 5.3 considers also the exponential fit. Another quality check of the fit is the χ^2/NDF which is 11 for the polynomial fit and 16 for the exponential fit. Both values are not good. Nevertheless, the polynomial fit is preferred here as well.
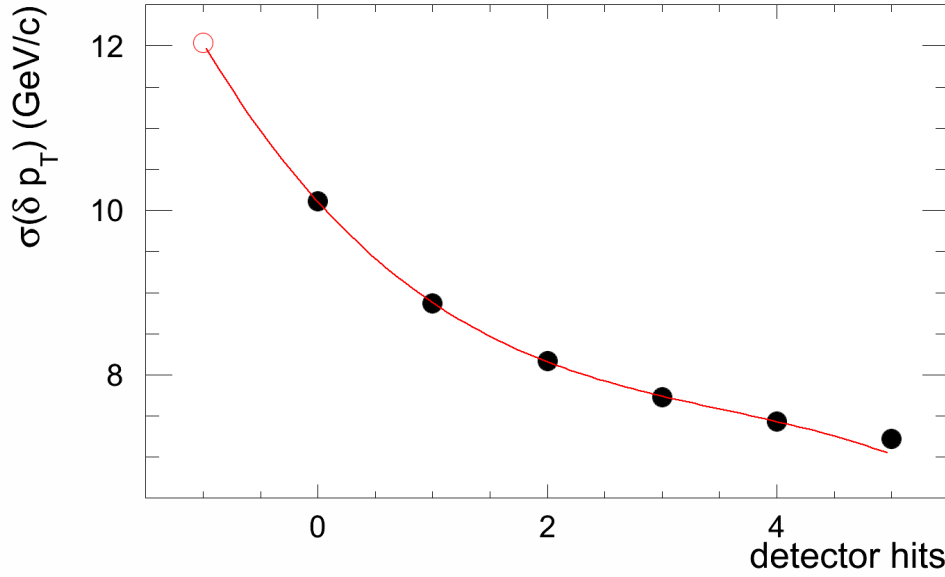
Figure 5.2.: Back-extrapolation of $\sigma(\delta p_T)$ for LHC11h data with $3.3 \cdot 10^6$ events. For the fit the points from zero to four detector hits are used. The values are described in the text.

5.2. Back-Extrapolation of 2011 Data

The data used in this section is from the period LHC11h and available online (see [Zimb]). All runs are displayed in the appendix in Table B.3. An advantage of the 2011 data set is the much bigger statistics of $3.3 \cdot 10^6$ events. A trigger for central events with $0 - 10\%$ centrality was used besides the normal minimum bias data taking.

However, the 2011 data also has a disadvantage. The Quality Assurance (QA) is not as good as the one for 2010 until now. This means there may be runs in the analysis where single detectors or parts of a detector did not work properly. This leads to bigger uncertainties and deviations as usual.

With this data, the same analysis as in the previous section was done. The 2011 p_T dependent efficiency was used for this. It is displayed in the appendix in Figure D.1. Strong fluctuations seen for high p_T, which will be understood with more QA studies, are in this spectrum. At low p_T, the efficiency is very similar to the 2010 efficiency, and Figure 4.2 indicates that the most particles have this energy. The φ dependent efficiency is again used from 2010 because the efficiency for 2011 was not available. The back-extrapolation of the 2011 data is shown in Figure 5.2. While the measured $\sigma(\delta p_T) = (10.108 \pm 0.004)\,\mathrm{GeV}/c$ is a little bit lower (difference: -0.057 GeV/c) than the 2010 one, the back-extrapolation provides a higher result of $\sigma(\delta p_T) = (12.034 \pm 0.017)\,\mathrm{GeV}/c$ (difference: $0.217\,\mathrm{GeV}/c$).

Here the $\chi^2/NDF = 41$ is very bad. The alternative with the exponential fit is even

worse with $\chi^2/NDF = 58$. A comparison of the different fits is done in more detail in the systematic uncertainty (cf. Section 5.3).

There is a difference of $0.217\,\mathrm{GeV}/c$ between the 2010 and 2011 back-extrapolation. This is not within the expected uncertainty, which was calculated to $\Delta_{\mathrm{syst}}^{sim}\sigma(\delta p_T) = 0.05\,\mathrm{GeV}/c$ in the simulations in Section 4.5. The difference of the 2010 and 2011 measured $\sigma(\delta p_T)$ of $0.057\,\mathrm{GeV}/c$ does not need to be considered for the comparison of the back-extrapolated values, because the different measured standard deviations are a consequence of the different detector effects.

In the next section, the systematic uncertainty of the data is reevaluated. As a result, the systematic uncertainty covers the whole difference of the 2010 and 2011 back-extrapolation.

5.3. Systematic Uncertainties

The systematic uncertainty was already calculated to $\Delta_{\mathrm{syst}}^{sim}\sigma(\delta p_T) = 0.05\,\mathrm{GeV}/c$ in the simulation Section 4.5. Here the uncertainty of the detector hit method (a rotating or a normal detector, a dependent or an independent detector hit) should not be repeated. However, the uncertainty of the fitting process, the usage of different fitting functions and the usage of a different number of fitting points are analyzed again. The uncertainties of the simulation ($0.025\,\mathrm{GeV}/c$ for the rotating detector and $0.031\,\mathrm{GeV}/c$ for the dependent simulation) are used for the uncertainty of the detector hit method. The polynomial back-extrapolation with fife points was already shown in Figure 5.1. In Figure 5.3, the back-extrapolation with the exponential function is displayed. With a $\sigma(\delta p_T) = (11.932 \pm 0.020)\,\mathrm{GeV}/c$ the result of the back-extrapolation is $0.115\,\mathrm{GeV}/c$ higher than the polynomial result. As already mentioned in Section 5.1, the $\chi^2/NDF = 16$ is worse than the one for the polynomial fit function.

Like the fits before, the polynomial fit function with six points has a bad $\chi^2/NDF = 20$. The result is with $\sigma(\delta p_T) = (11.723 \pm 0.019)\,\mathrm{GeV}/c$ about $0.094\,\mathrm{GeV}/c$ lower than the back-extrapolation of five points.

All results of the back-extrapolations are displayed in the appendix in Table F.1. In Table 5.1, all deviations for the 2010 data analysis are summarized.

method	deviation 2010	deviation 2011
fit points	0.094	0.311
fit function	0.115	0.198
rotating	0.025	0.025
dependent	0.031	0.031
$\Delta_{\mathrm{syst}}^{2010/2011}\sigma(\delta p_T)$	0.154	0.371

Table 5.1.: Deviation between the back-extrapolated points for different approaches in 2010 and 2011 data. The comparison is always done with respect to the nominal value for polynomial fit and six points. The detector hit methods rotating and dependent are adopted from Section 4.5.
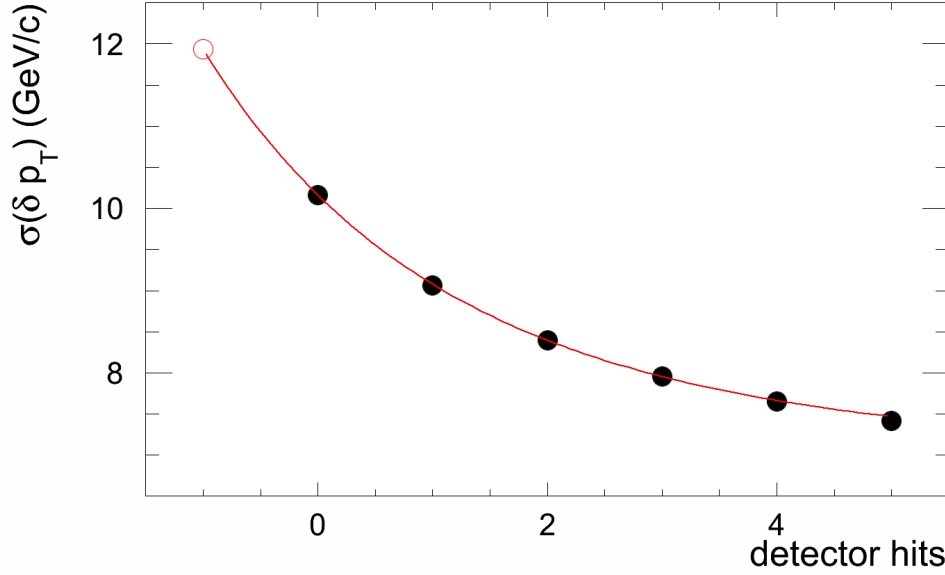
Figure 5.3.: Back-extrapolation of $\sigma(\delta p_T)$ for LHC10h data. Here the points from 0 to 4 detector hits are fitted with the exponential function from Equation 4.4. The measured standard deviation of $\sigma(\delta p_T) = (10.165 \pm 0.019)\,\text{GeV}/c$ is corrected with the exponential fit function to $\sigma(\delta p_T) = (11.932 \pm 0.024)\,\text{GeV}/c$.

Again, the systematic uncertainty is calculated as the square root of the squared sum of all deviations. The result is $\Delta_{\text{syst}}^{2010}\sigma(\delta p_T) = 0.15\,\text{GeV}/c$. This is nearly twice as large as expected from the simulation. Here the rotating detector no longer dominates the systematic uncertainty. These results show that the uncertainty of the HBOM method is quite bigger than supposed. A further investigation of the uncertainty may be done. One natural explanation is that correlations which are not part of the fast simulation have an impact in the real data. The deviation of the rotating and dependent detector could also be calculated again with the data. However, this is not done here. In any case the found systematic uncertainty is a good basis for the uncertainty estimation. Besides this analysis of the 2010 data, the systematic uncertainty could also be calculated for the 2011 data. All deviations are also shown in Table 5.1. The systematic uncertainty rises to $\Delta_{\text{syst}}^{2011}\sigma(\delta p_T) = 0.37\,\text{GeV}/c$ and is dominated by the fit points. Because of the worse QA of the 2011 data, a bigger systematic uncertainty for 2011 data than for 2010 was already expected.

Within this systematic uncertainty, the back-extrapolation of the 2010 and 2011 standard deviation agree with each other. The determined values are:

$$2010: \sigma(\delta p_T) = (11.82 \pm 0.03\,(\text{stat}) \pm 0.15\,(\text{syst}))\,\text{GeV}/c$$
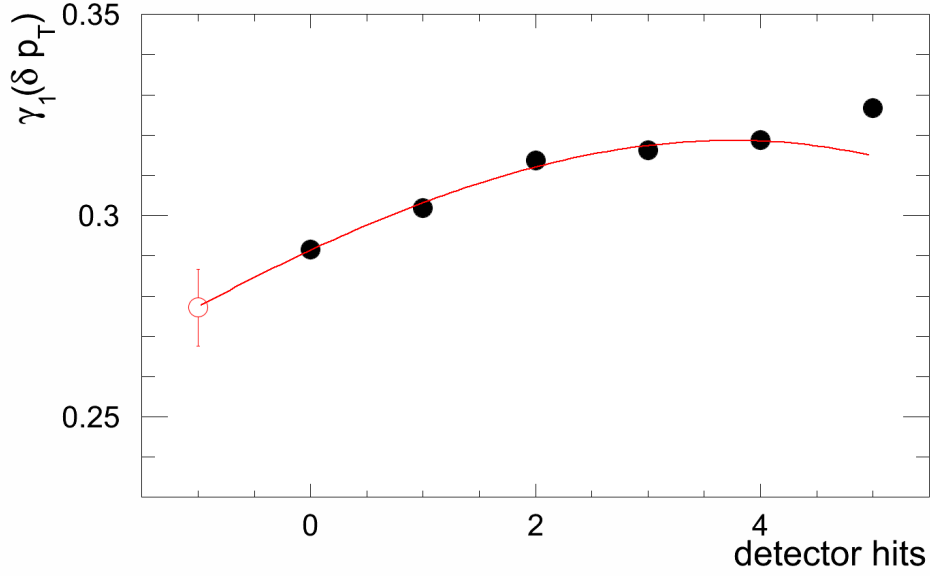$$2011: \sigma(\delta p_T) = (12.03 \pm 0.02\,(\text{stat}) \pm 0.37\,(\text{syst}))\,\text{GeV}/c.$$
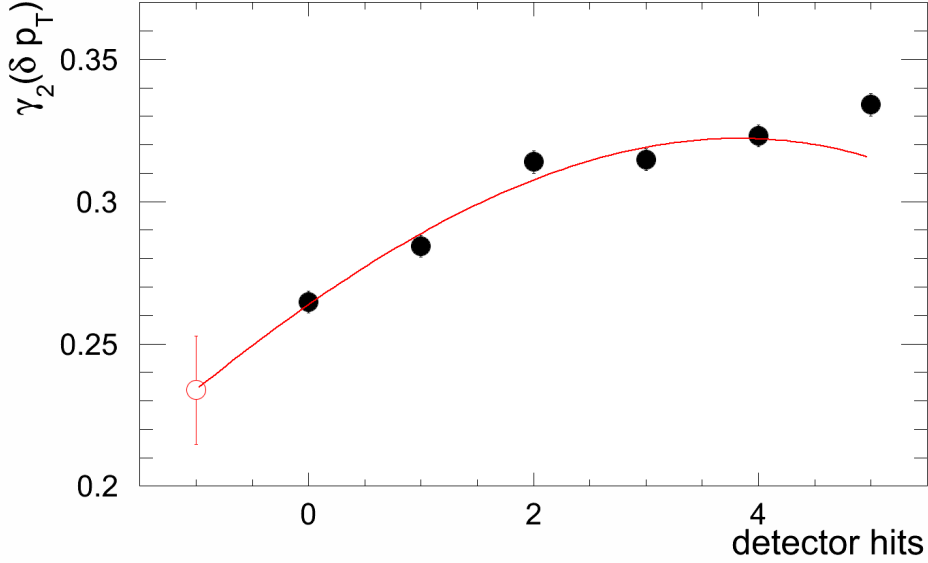
Figure 5.4.: Back-extrapolation of the skewness $\gamma_1(\delta p_T)$ for LHC10h data. For the fit, up to four detector hits are used. The measured and back-extrapolated values are displayed in Table 5.2.

The standard deviations should be identical. They describe the same physical observable. Consequently, the average standard deviation with the standard weighted least-squares procedure is calculated. The weighting is done with the systematic error.

$$\sigma(\delta p_T) = (11.85 \pm 0.14)\,\text{GeV}/c.$$

5.4. Higher Moments

The higher moments of the δp_T distribution can also be back-extrapolated for the data. In Figure 5.4, the back-extrapolation of the skewness for the LHC10h data is shown. Attention should be paid to the much lower scale compared to the standard deviation. Here the $\chi^2/NDF = 1.5$ shows that the fit has a better quality than the fit for the $\sigma(\delta p_T)$.

With five points, the back-extrapolation of the skewness works well for the data analysis. The usage of six points provides a little lower skewness, and the fit has the same χ^2. In Table 5.2, the measured and back-extrapolated skewnesses are displayed. For 2010, the mean skewness is calculated to $\gamma_1(\delta p_T) = (0.272 \pm 0.006)\,\text{GeV}/c$ with the standard weighted least-squares procedure.

This is much higher than the simulated skewness of $\gamma_1(\delta p_T) = (0.225 \pm 0.002)\,\text{GeV}/c$. But as explained in Section 5.1, the simulation does not include all effects that are present in data. A consequence of this is the larger $\sigma(\delta p_T)$ in data than in the simulation.

points	2010 $\gamma_1(\delta p_T)$	χ^2/NDF	2011 $\gamma_1(\delta p_T)$	χ^2/NDF
measured	0.292 ± 0.002		0.293 ± 0.001	
5	0.277 ± 0.010	1.5	0.262 ± 0.007	0.42
6	0.269 ± 0.007	1.5	0.272 ± 0.005	2.5
mean	0.272 ± 0.006		0.269 ± 0.006	

Table 5.2.: Back-extrapolated skewnesses for different number of points which are used for the back-extrapolation.

Figure 5.5.: Back-extrapolation of the kurtosis $\gamma_2(\delta p_T)$ for LHC10h data. For the fit, up to four detector hits are used. The measured and back-extrapolated values are displayed in Table 5.3.

The skewness is also higher. There are true jet correlations in the data which lead to a larger jet tail of the δp_T distribution. This jet tail causes a larger width and a larger asymmetry of the spectrum. The larger width is already expressed by the standard deviation; the larger asymmetry is shown by the skewness.

The 2011 data provides another comparative value. The skewness of the 2011 data is shown in the appendix in Figure E.1. Again, the fit with five points is possible, but the $\chi^2/NDF = 0.42$ is better than expected. This may indicate that this extrapolation is not optimal. Consequently, the back-extrapolation for the 2011 data is also done with six points. The results of all back-extrapolations are displayed in Table 5.2. For 2011 data, the mean skewness is calculated to $\gamma_1(\delta p_T) = (0.269 \pm 0.006) \,\mathrm{GeV}/c$. The mean skewness of 2010 and 2011 agree well with each other within their error bars.

The back-extrapolation was tried again for the kurtosis. In the simulations it was very difficult, but it works for the data analysis. In Figure 5.5, the back-extrapolation of

the LHC10h kurtosis is shown. The $\chi^2/NDF = 5.4$ indicates an acceptable fit, but the point at two detector hits is quite far away from the other points. To check the result, the back-extrapolation is also done with six points. Again, all results are determined for 2010 and 2011 and are displayed in Table 5.3.

points	2010 $\gamma_2(\delta p_T)$	χ^2/NDF	2011 $\gamma_2(\delta p_T)$	χ^2/NDF
measured	0.264 ± 0.004		0.279 ± 0.003	
5	0.234 ± 0.019	5.4	0.216 ± 0.013	0.50
6	0.221 ± 0.014	3.2	0.235 ± 0.010	2.5
mean	0.226 ± 0.011		0.228 ± 0.008	

Table 5.3.: Back-extrapolated kurtoses for different number of points which are used for the back-extrapolation.

The back-extrapolation for the LHC11h data is not shown here, but is displayed in the appendix in Figure E.2. The 2011 analysis, just like the 2010 analysis, uses a back-extrapolation for fife and six points. The mean kurtosis is calculated with the standard weighted least-squares procedure. Within the error bars, the corrected values of the 2010 and 2011 data agree. This agreement shows that the correction is more reliable than assumed from the simulations.

For the skewness as well as for the kurtosis, one final mean can be calculated with the 2010 and 2011 values:

$$\gamma_1 = 0.270 \pm 0.003$$
$$\gamma_2 = 0.227 \pm 0.006$$

5.5. Back-Extrapolation of the δp_T Distribution

After back-extrapolating single observables of the δp_T distribution, the whole distribution is corrected. Section 4.7 showed that the smearing correction is better than the bin-by-bin correction, but both methods are again presented here. It is expected to obtain better results from the smearing correction, and the analysis in this section does not refute this.

First the 2010 data is corrected. In Figure 5.6, the measured (red triangles), the smeared corrected (blue squares) and the bin-by-bin corrected (green circles) distribution are shown. For the smeared correction, the back-extrapolated $\sigma_{HBOM}(\delta p_T) = 11.817\,\text{GeV}/c$ determined in Section 5.1 is used. Both corrected distributions are identical for the area around $\delta p_T = 0$ and outside of this area ($p_T < -20$ and $p_T > 30$), the bin-by-bin corrected distribution drops under the smeared corrected one. This is the same result as the correction of the simulated spectrum in Section 4.7. Consequently, it is expected to obtain a good corrected spectrum with the smeared correction.

In Figure 5.7, the correction of the 2011 δp_T distribution is shown. The used symbols mean the same as in the 2010 correction. For the smearing correction, the back-
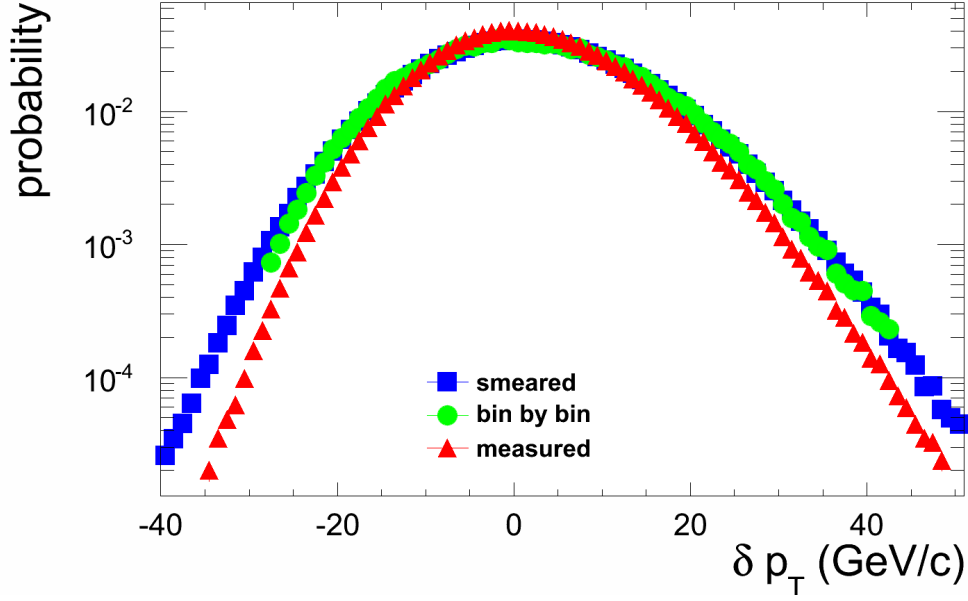
Figure 5.6.: Measured δp_T distribution (red triangles) of LHC10h data together with the smeared (blue squares) and the bin-by-bin (green circles) corrected distribution. The smeared one aims to $\sigma_{HBOM}(\delta p_T) = 11.817 \, \text{GeV}/c$ and the bin-by-bin distribution provides $\sigma = (11.552 \pm 0.032) \, \text{GeV}/c$.

extrapolated $\sigma_{HBOM}(\delta p_T) = 12.034 \, \text{GeV}/c$ is used. Again, the smeared distribution is a bit higher than the bin-by-bin distribution at $|p_T| > 20 \, \text{GeV}/c$.

Summary

The HBOM method can correct the detector effects for data. This is shown for the background fluctuations in the δp_T distribution. First, only the standard deviation $\sigma(\delta p_T)$ is corrected, and then the higher moments are also corrected. At last the whole distribution is corrected. The first detector effect corrected δp_T distributions are shown here.

The results of the different approaches agree within their error bars. However, the systematic uncertainty is larger than expected from the simulation.
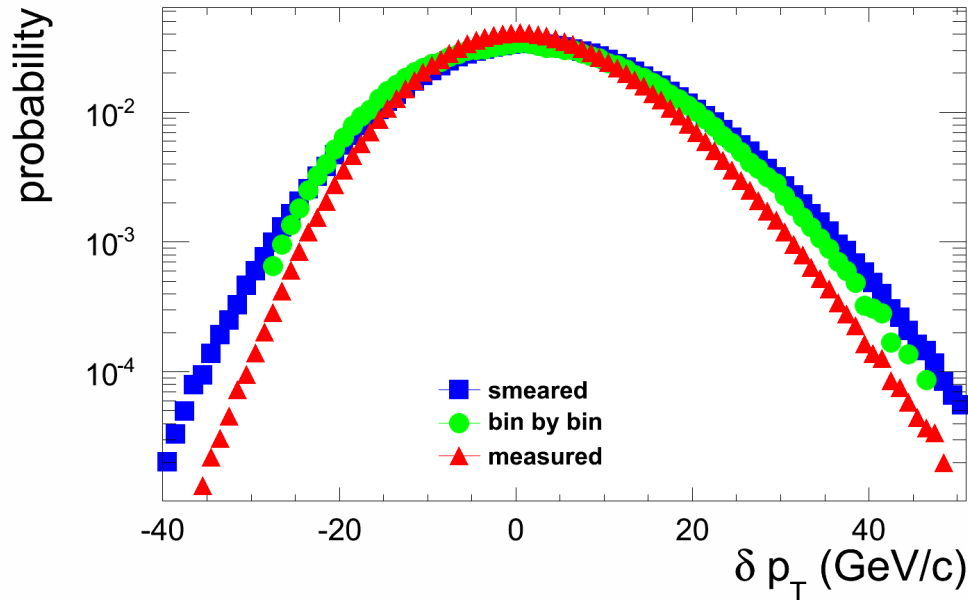
Figure 5.7.: The same analysis as in Figure 5.6 for 2011 data. The smeared correction aims to $\sigma_{HBOM}(\delta p_T) = 12.034\,\mathrm{GeV}/c$ and the bin-by-bin distribution provides $\sigma = (11.713 \pm 0.022)\,\mathrm{GeV}/c$.
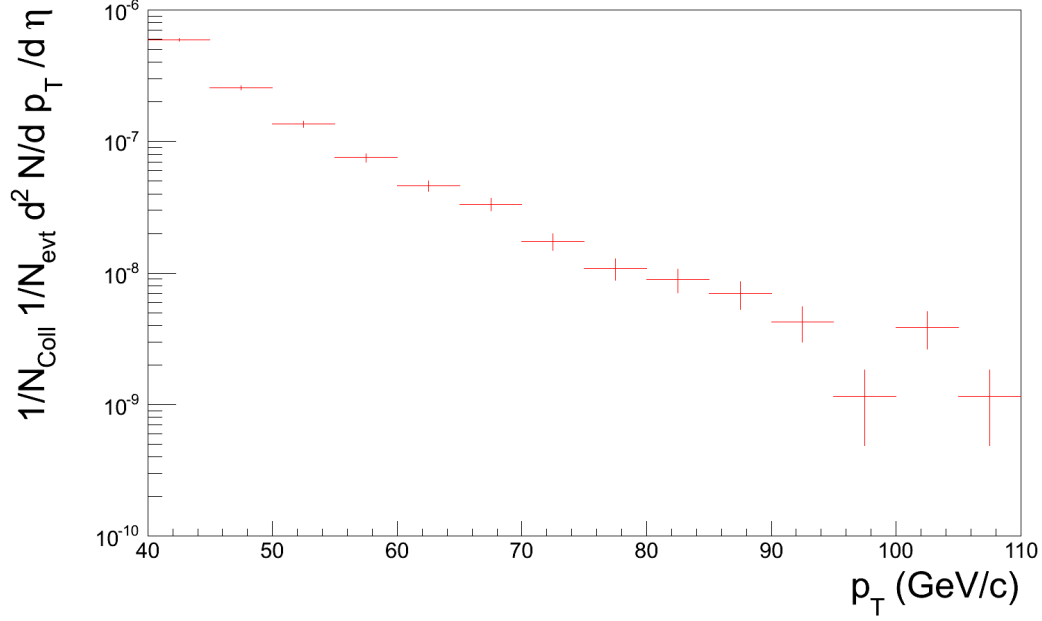
6. Unfolding of the Jet Spectrum

Figure 6.1.: Part of the 2010 charged raw jet spectrum which is unfolded in this section. It is obtained with the anti k_t jet finder at $R = 0.3$ and $p_{T,min} = 0.15\,\mathrm{GeV}/c$ at a centrality of $0-10\%$. The used Pb-Pb data is available online at [KBb] and the runs are displayed in the appendix in Table B.1.

The ALICE jet spectrum, determined with the anti k_t jet finder at $R = 0.3$ and $p_{T,min} = 0.15\,\mathrm{GeV}/c$ at a centrality of $0 - 10\%$, is shown in Figure 6.1. This spectrum should be corrected for the background fluctuations and the detector effects. For this, the response matrix is build up from two matrices. The first part is the background fluctuation $\mathbf{R}_{\delta p_T}$ and the second part is the detector effects $\mathbf{R}_{\det}$. The background fluctuations are implemented by filling the response matrix for each "true" bin with the δp_T distribution centered around the same measured bin. The measured δp_T distribution determined with the radius $R = 0.3$ is used for the unfolding. This is done because the unfolding process for 2010 data does not provide good results for bigger radii. In Figure 6.2, the resulting fluctuations response matrix $\mathbf{R}_{\delta p_T}$ is presented. The binning of the response matrix is adapted to the measured and the designed unfolded spectrum. This coarse binning is used because only this binning is needed in the multiplication, and a finer binning would lead to unphysical fluctuations. While the
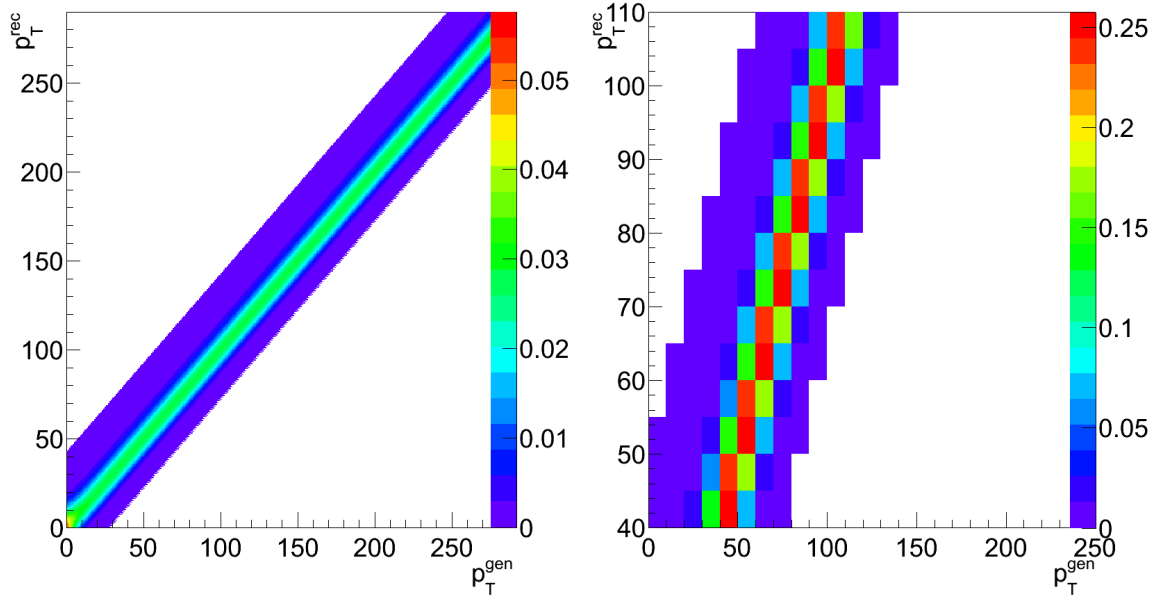
Figure 6.2.: In the left panel, the fluctuations response matrix $\mathbf{R}_{\delta p_T}$ in the fine binning is shown. This matrix is made by putting the measured δp_T distribution into each generated bin. The used δp_T distribution was determined with a radius of $R = 0.3$ at a centrality of $0 - 10\%$. In the right panel, the coarse binned matrix is adapted to the binning of the jet and the unfolded spectrum (cf. [Ver12]).

reconstructed y-axis has the same binning as the measured spectrum, the generated x-axis should have a coarse binning. In the following section, the reason for the coarse binning is described.

The unfolded spectrum is multiplied with the response matrix, and the folded spectrum is compared to the measured spectrum. This comparison is done for m points of the folded and the measured spectrum. The input of the folded spectrum is the unfolded one, which should have a larger p_T range as the considered range and simultaneously less points than m. A larger range is needed because of the response matrix, which shifts points from outside the considered range into it. This is especially important for the jet spectrum, which is a strongly falling spectrum. Here a non-negligible part of the spectrum is fed in from lower p_T into the range in which the measured and folded spectrum are compared. The number of points of the unfolded spectrum represents the degrees of freedom. If these are equal or greater than the number of bins in the measured range m, the unfolding process breaks down. In this thesis, the bin widths of the unfolded bins are chosen to be twice the bin width of the measured bins. This bin width from the unfolded bins defines the x-axis of the response matrices.

Additional effects which change the "true" spectrum are the detector effects, e. g. the jet energy is smeared or particles with low energy are not detected. The detector effect
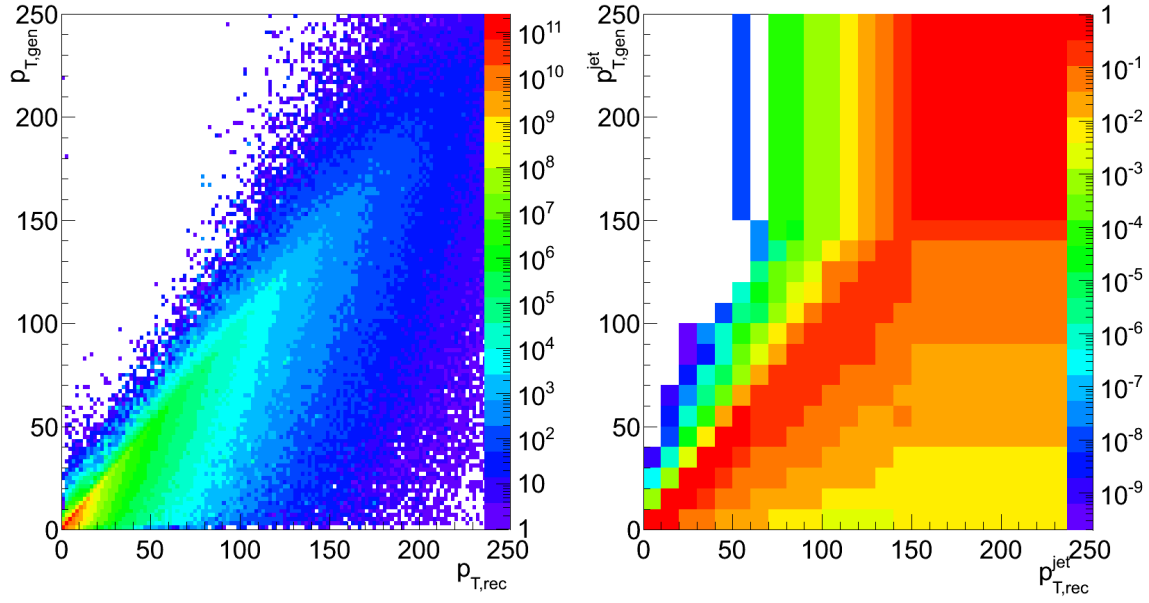
Figure 6.3.: In the left panel the detector response matrix $\mathbf{R}_{\mathrm{det}}$ in the fine binning for a radius of $R = 0.3$ and a centrality of $0 - 10\%$ is shown. In the right panel the coarse binned matrix is displayed [Ver12].

matrix $\mathbf{R}_{\mathrm{det}}$ is taken from [Ver12] and shown in 6.3. In the left panel, it has a fine binning and in the right one, a coarse binning. The matrix was created for the radius $R = 0.3$ and $0 - 10\%$ centrality.

Either both detector effects could be corrected one after the other, or both detector matrices are multiplied and then one correction is done. Equation 2.11 goes into Equation 6.1, which shows the full correlation of the measured and the "true" spectrum

$$M = \mathbf{R}_{\delta p_T} \cdot \mathbf{R}_{\mathrm{det}} \cdot T. \tag{6.1}$$

The combined response matrix $\mathbf{R}_{\mathrm{com}} = \mathbf{R}_{\delta p_T} \cdot \mathbf{R}_{\mathrm{det}}$ is shown in Figure 6.4. The efficiency to detect a jet is also displayed there. This efficiency shows that jets with a momentum lower than $50 \, \mathrm{GeV}/c$ are improbably detected. If they are detected, the response matrix shows that the reconstructed jet often has more energy than the real jet really had.

With the combined response matrix, the jet spectrum in Figure 6.1 is unfolded in the p_T range between 40 and $110 \, \mathrm{GeV}/c$. In this range the best statistic is available. Different regularization strengths β (cf. eq. 2.12) were tested for the unfolding. The lowest and highest β which provide continuous results are shown in Figure 6.5. As mentioned above, the unfolding is done in a broader p_T range than the measured spectrum because the response matrix shifts jets into the measured range. As a reference, unfolded jet spectra from [Ver12] are displayed in addition. Both spectra should be identical because they are calculated with the same method and the same data. For the small $\beta = 4.55 \cdot 10^{-5}$ the error bars are quite high outside the used p_T
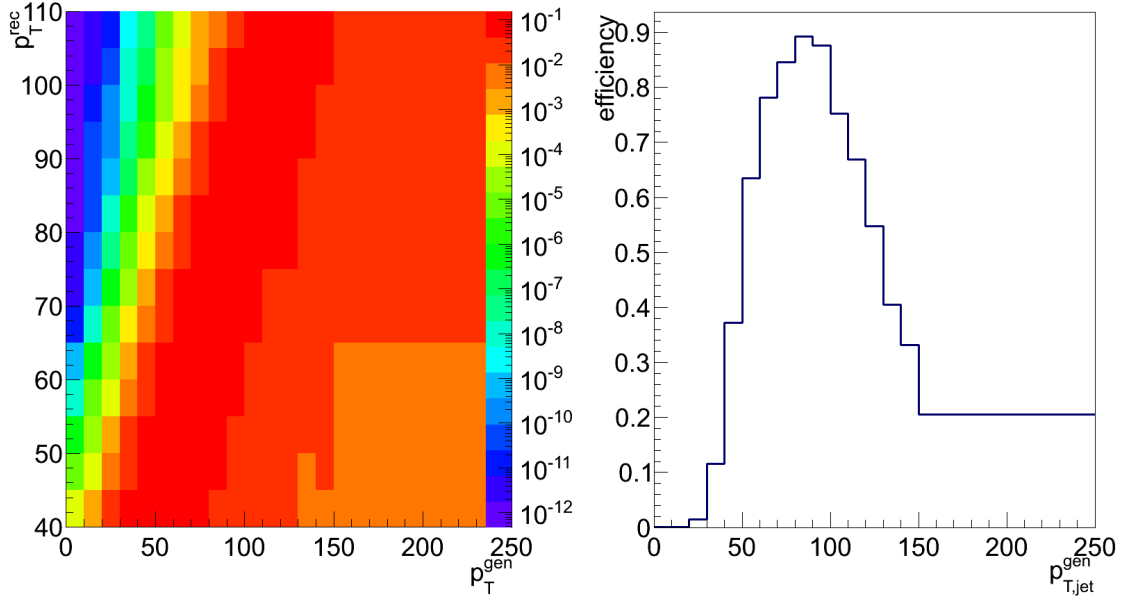
Figure 6.4.: In the left panel, the combined response matrix $\mathbf{R}_{\mathrm{com}}$ for the radius $R = 0.3$ and the centrality $0 - 10\%$ is shown. In the right panel, the detection efficiency is shown. It is the integrated p_T^{rec} of the combined response matrix on the left panel (cf. [Ver12]).

range. Nevertheless, the unfolded spectrum and the reference spectrum agree with each other. The low β are the minimum β which provide reasonable continuous results. In contrast, the high β are the maximal values which provide a folded spectrum which agrees with the measured one.

In Figure 6.6, a zoom into the p_T range of 40 to $110\,\mathrm{GeV}/c$ is shown. It can be seen that the unfolded values are a little bit higher than it would be expected from the reference values [Ver12]. But within the error bars, the unfolded and the reference spectra agree for the p_T range of 40 to $110\,\mathrm{GeV}/c$. Outside of this range, the results differ much more, but there they are less based on the measured data. Compared to the measured spectrum (cf. Figure 6.1) both the unfolded and the reference spectra are very different. Under consideration of this difference, the unfolded and reference spectra are very similar.

As mentioned earlier, both spectra are calculated with the same unfolding procedure. Consequently, the result should also be the same. Only the used response matrices are a little bit different. They have the same binning, so it is easy to compare them. In the highest p_T^{rec} bin $100 - 110\,\mathrm{GeV}/c$, the bin content of the reference matrix is a little bit higher. In all other bins, the difference of the bin content is negligible compared with the error of the bins. In addition, the difference is only a tenth of the error bar in the highest bin. This shows that relatively small changes in the response matrix can lead to observable differences in the unfolded spectra. This interesting fact should be
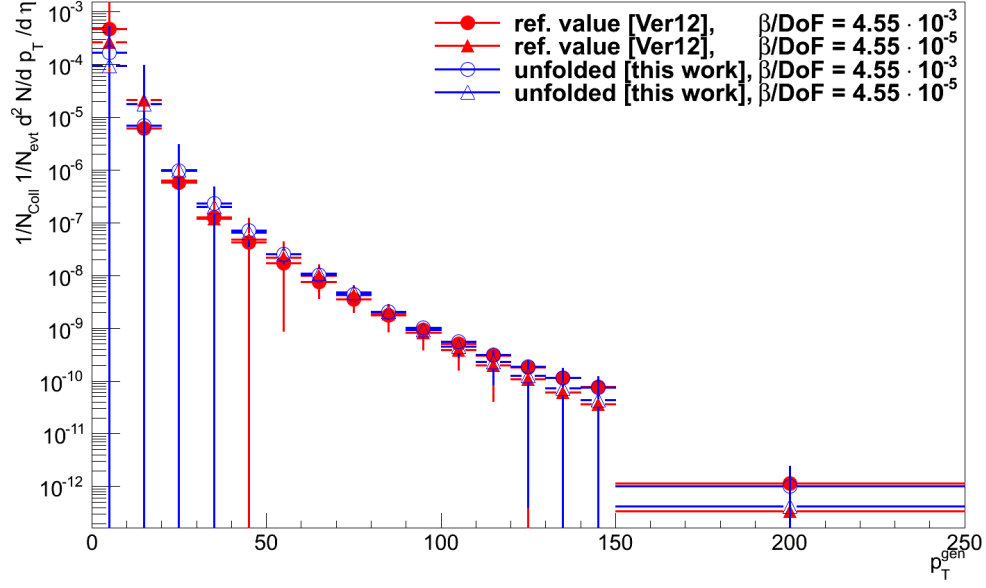
Figure 6.5.: Unfolded jet spectra produced with $R = 0.3$, $p_{T,min} = 0.15\,\mathrm{GeV}/c$ and different β per degree of freedom (DoF). Reference values from [Ver12] are shown in red. The unfolded spectra in blue are produced with the raw jet spectrum in Figure 6.1 and the response matrix in Figure 6.4. A zoom into the p_T range of 40 to $110\,\mathrm{GeV}/c$ is shown in Figure 6.6.
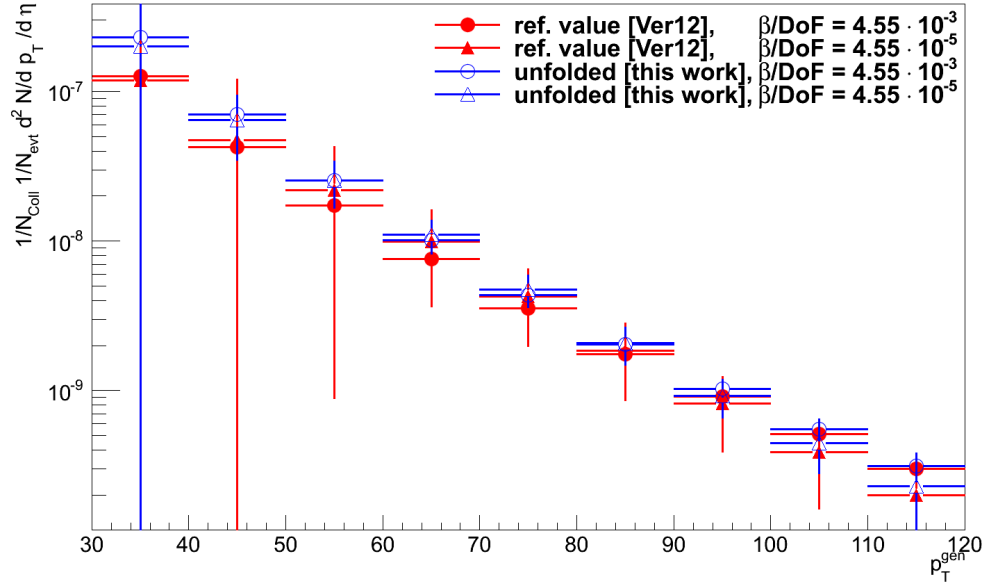

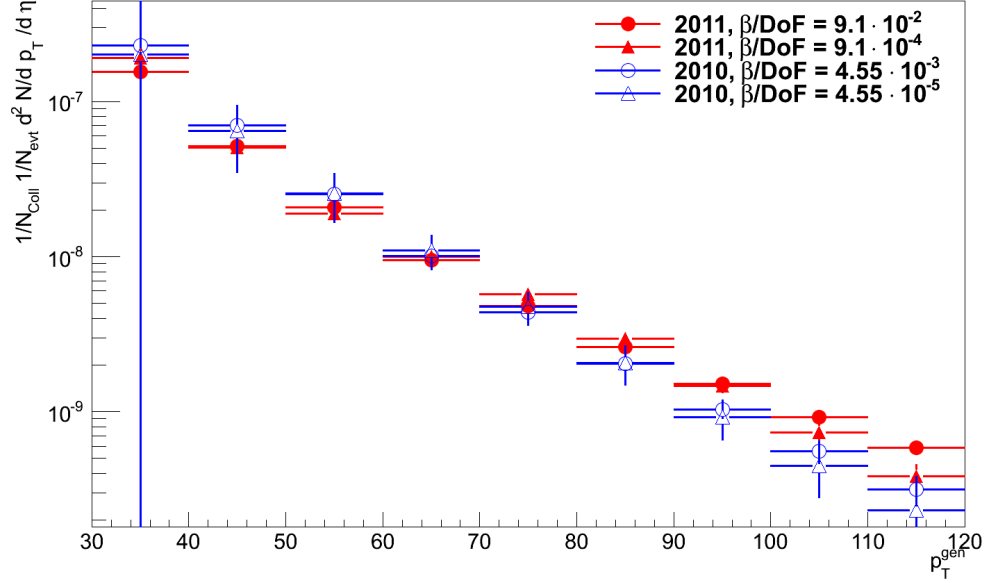Figure 6.6.: Zoom into the p_T range of 40 to $110\,\mathrm{GeV}/c$ of Figure 6.5.

Figure 6.7.: Comparison of the 2010 and 2011 unfolded jet spectra. The jet spectra are created with a search radius $R = 0.3$ and a minimum transverse momentum $p_{T,min} = 0.15\,\mathrm{GeV}/c$. For the 2011 unfolding the β/DoF is a little bit higher than for the 2010 unfolding to get continuous results and an agreement of the folded and measured spectrum. These results could only be seen as an outlook for further analysis, because different pre-analysis are not fully validated until now.

investigated further, however, it is not part of this thesis.

Besides the 2010 jet spectrum, the 2011 jet spectrum can be analyzed. However not all the QA checks are done and the centrality is not flat as it is for 2010. This can lead to bigger errors in the jet spectrum and consequently to bigger errors in the unfolding. In addition, the unfolding analysis is only done the same way as for 2010. Besides the β, different p_T ranges and search radii could also be analyzed. Consequently, this 2011 data analysis should only be seen as an outlook for the future.

The 2011 jet spectrum (available online at [KBd] with $R = 0.3$ and $p_{T,min} = 0.15\,\mathrm{GeV}/c$), presented in the appendix in Fig G.1, is corrected with the response matrix build up with the δp_T distribution for 2011 (available online at [KBc] with $R = 0.3$ and $p_{T,min} = 0.15\,\mathrm{GeV}/c$) and the detector response matrix from Figure 6.3. The used runs from the 2011 data are displayed in the appendix in Table B.2. The result of the unfolding is displayed in Figure 6.7 and compared with the 2010 results described above. For the unfolding process, the same setting is used.

Obviously, the results are not identical. The 2011 spectrum is flatter than the 2010 one. For further analysis, the QA checks have to be done and the centrality has to be validated. If these pre-analysis are done, more detailed unfolding analysis could be

done.

In principle, it should also be possible to do the unfolding correction of the jet spectrum with the HBOM method. But to do this, different further analysis must be done first. For example after a detector hit either the place of a jet could be held or the jet-finder could search again for the jets. Different search radii R and track momentum cut offs $p_{T,min}$ should also be tested. The jet spectrum has a completely other shape as the δp_T spectrum, so the best detector hit method and fitting method may be different from the one used in this thesis.

7. Summary and Outlook

The main focus of this work has been the correction of jet related observables in heavy-ion collisions. This is important for the comparison between experiments and theory.

The HBOM method is a method which is able to determine corrected measured values via extrapolation without the need for a detailed simulation. The principle problem of a detailed simulation is that not all correlations can be known. There are always a few correlations that cannot be described or have not yet been discovered. One big advantage of the HBOM method is that it does not need the information about these correlations.

The method is validated in simulations that emulate the generic features of heavy-ion collisions such as the multiplicity, the p_T spectrum or flow. In these simulations, the extrapolated values can be compared with the original simulated values without detector effects to optimize the application of the HBOM method. On this basis, the fixed detector and the independent efficiency application have been chosen. As best fitting procedure a polynomial fit of third order with five fitting points has been determined. With this configuration, a simulated standard deviation of $\sigma(\delta p_T) = (9.43 \pm 0.02\,(\text{stat}) \pm 0.05\,(\text{syst}))\,\text{GeV}/c$ is achieved for the centrality $0 - 10\%$ and the "true" value of $\sigma(\delta p_T) = (9.458 \pm 0.005)\,\text{GeV}/c$ is reproduced.

After the validation of the method, the analysis is done with Pb-Pb collision data from two run periods (2010 and 2011). A comparison with the simulated value was not possible because the simulation does not consider all correlations. As consequence the simulated values are much lower than the ones from data. However, the results of the 2010 and 2011 data analysis could be compared with each other. The results are for centrality $0 - 10\%$:

$$2010: \sigma(\delta p_T) = (11.82 \pm 0.03\,(\text{stat}) \pm 0.15\,(\text{syst}))\,\text{GeV}/c$$
$$2011: \sigma(\delta p_T) = (12.03 \pm 0.02\,(\text{stat}) \pm 0.37\,(\text{syst}))\,\text{GeV}/c.$$

While the statistics of the 2011 data are larger, resulting in a smaller statistical uncertainty, so far the 2010 data has been better evaluated in terms of uniform data quality, resulting in a smaller systematical uncertainty. Within the uncertainties, the results agree. This shows that the HBOM method is a consistent method of correcting observables for their detector effects. Both results could be combined to one value for the standard deviation of the δp_T distribution:

$$\sigma(\delta p_T) = (11.85 \pm 0.14)\,\text{GeV}/c.$$

In the future, this analysis should be expanded to different centralities and other minimum track momenta $p_{T,min}$. Here, the systematic uncertainties need to be re-evaluated

with a data driven analysis of the detector hit method.

Besides the correction of one observable, the whole δp_T distributions has also been corrected. Here, the smearing method, in which the δp_T distribution is convoluted with a scaled copy of itself, provided the best results. It has a broader p_T range, in which it is able to correct the δp_T distribution, than a bin-by-bin HBOM extrapolation method. Consequently the δp_T distribution is corrected for the detector effects with the smearing method.

At the end of this thesis, the unfolding of the jet spectrum was presented. It is the standard procedure for correcting a spectrum for its detector effects. The unfolded results for 2010 agree with ALICE preliminary results within the error bars.

As an outlook, the first unfolding results for the 2011 data are presented. These are only based on the first results of the underlying analysis and therefore they require more studies.

In the future, the HBOM method could also be used as an alternative to the unfolding.

This thesis showed the possibility of correcting observables for their detector effects without knowing the correlations in the event. Thus, the analysis of observables in events with correlations, which are not understood or which are only describable with large uncertainties, can be improved. The HBOM analysis provides an important alternative to more simulation based corrections, in particular for observables that depend on a priori unknown event properties.

A. Detector Hit Methods

configuration	$\sigma_{\mathrm{norm}}(\delta p_T)$ [GeV/c]	$\sigma_{\mathrm{rot}}(\delta p_T)$ [GeV/c]	$\sigma_{\mathrm{dep}}(\delta p_T)$ [GeV/c]
simulated	9.458 ± 0.005	9.473 ± 0.005	9.461 ± 0.005
measured	8.330 ± 0.005	8.331 ± 0.005	8.321 ± 0.005
extrapolated	9.449 ± 0.020	9.424 ± 0.020	9.418 ± 0.020
χ^2/NDF	2.2	40	0.05

Table A.1.: The simulated, measured and polynomial back-extrapolated values of the standard deviation $\sigma(\delta p_T)$ for different detector hit methods. The χ^2/NDF belongs to the polynomial back-extrapolation.

B. List of analyzed Data Sets

In this appendix the data sets used in the analysis are listed. Each table corresponds to one train.

run number	Accepted data sets
31	137439, 137443, 137530, 137531, 137541, 137544, 137546, 137595, 137608, 137638, 137639, 137685, 137691, 137693, 137724, 137848, 138438, 138652, 138730, 138732, 138872, 139028, 139029, 139036, 139037, 139038, 139105, 139309, 139310, 139314, 139328, 139329, 139360, 139503, 139505, 139510
26	137161, 137162, 137231, 137232, 137235, 137236, 137243, 137366, 137430, 137431, 137432, 137434, 137439, 137440, 137441, 137443, 137530, 137531, 137539, 137541, 137544, 137546, 137549, 137595, 137608, 137638, 137639, 137685, 137686, 137691, 137692, 137693, 137704, 137718, 137722, 137724, 137751, 137752, 137844, 137848, 138190, 138192, 138197, 138201, 138225, 138275, 138364, 138396, 138438, 138439, 138442, 138469, 138534, 138578, 138579, 138582, 138583, 138621, 138624, 138638, 138652, 138653, 138662, 138666, 138730, 138732, 138837, 138870, 138871, 138872, 139028, 139029, 139036, 139037, 139038, 139105, 139107, 139173, 139309, 139310, 139314, 139328, 139329, 139360, 139437, 139438, 139465, 139503, 139505, 139507, 139510

Table B.1.: List of data sets used in the Jets_PbPb train. All runs are Pb-Pb runs from LHC10h.

run number	Accepted data sets
15 and 20	167813, 167988, 168066, 168068, 168069, 168076, 168103, 168104, 168212, 168311, 168322, 168325, 168341, 168361, 168362, 168458, 168460, 168461, 168992, 169091, 169094, 169138, 169143, 169167, 169417, 169835, 169837, 169838, 169846, 169855, 169858, 169859, 169923, 169956, 170027, 170036, 170081

Table B.2.: List of data sets used in the Jets_PbPb_2011 train. All runs are Pb-Pb runs from LHC11h.

run number	Accepted data sets
15	167813, 167988, 168066, 168068, 168069, 168076, 168103, 168104, 168212, 168311, 168322, 168325, 168341, 168361, 168362, 168458, 168460, 168461, 168992, 169091, 169094, 169138, 169143, 169167, 169417, 169835, 169837, 169838, 169846, 169855, 169858, 169859, 169923, 169956, 170027, 170036, 170081
16	137161, 137162, 137231, 137232, 137235, 137236, 137243, 137366, 137430, 137431, 137432, 137434, 137439, 137440, 137441, 137443, 137530, 137531, 137539, 137541, 137544, 137546, 137549, 137595, 137608, 137638, 137639, 137685, 137686, 137691, 137692, 137693, 137704, 137718, 137722, 137724, 137751, 137752, 137844, 137848, 138190, 138192, 138197, 138201, 138225, 138275, 138364, 138396, 138438, 138439, 138442, 138469, 138534, 138578, 138579, 138582, 138583, 138621, 138624, 138638, 138652, 138653, 138662, 138666, 138730, 138732, 138837, 138870, 138871, 138872, 139028, 139029, 139036, 139037, 139038, 139105, 139107, 139173, 139309, 139310, 139314, 139328, 139329, 139360, 139437, 139438, 139465, 139503, 139505, 139507, 139510

Table B.3.: List of data sets used in the Jets_PbPb_AOD train. All runs are Pb-Pb runs. While run number 16 is from LHC10h, run number 15 is from LHC11h.

C. 2011 Multiplicity and p_T Spectrum

In Section 4.1, the 2010 multiplicity spectrum and 2010 p_T spectrum are used for the simulation. Besides this 2010 data, also the 2011 data is available. There is no reason why they should be different, and indeed they are identical. In this section the spectra are presented.
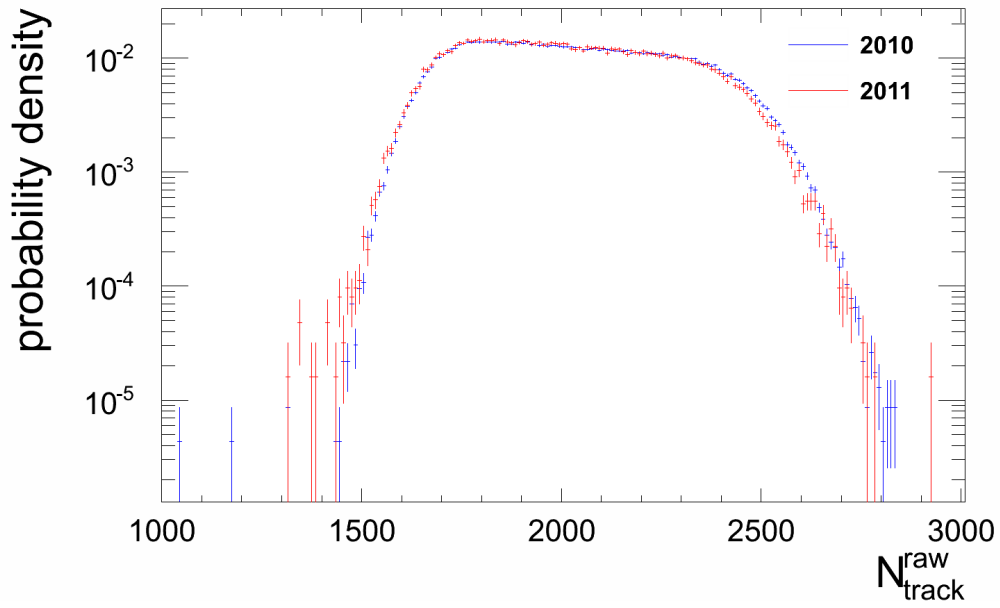

Figure C.1.: Comparison of the 2010 and 2011 multiplicity spectra for $0-10\%$ centrality. The spectra are based on the data available online at [KBa] and [KBd].
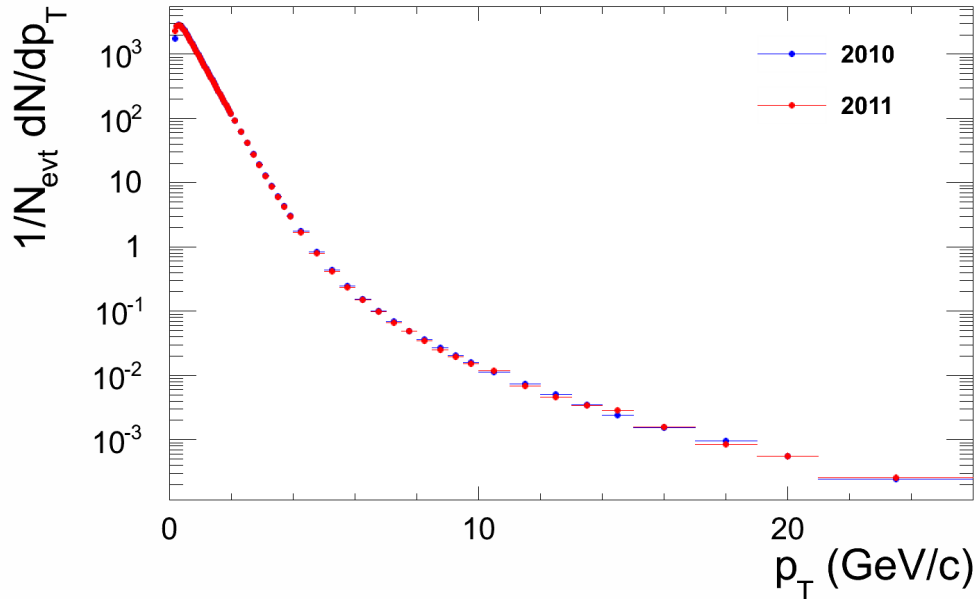
Figure C.2.: Comparison of the 2010 and 2011 particle spectra for $0 - 10\%$ centrality. The spectra both go up to $150\,\mathrm{GeV}/c$, but the probability of having a particle with more than $20\,\mathrm{GeV}/c$ in an event with up to $2800\,\mathrm{particles}$ is very small. The spectra are based on the data available online at [KBa] and [KBd].
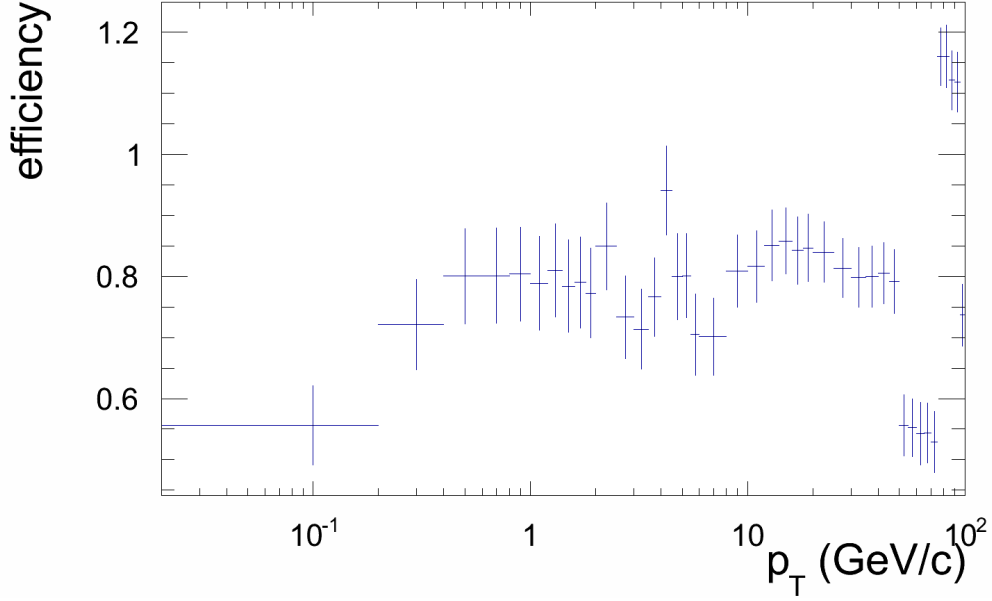
D. 2011 Efficiency

Figure D.1.: Single track efficiency ϵ_{Pb-Pb} to detect a particle in a Pb-Pb collision depending on the transverse momentum p_T of the particle for 2011 data. These values are determined from Monte Carlo simulations. The spectrum is available in AliRoot at OADB/PWGJE/HBOM/fastMCInput_LHC11h_120827.root in the revision 58316.
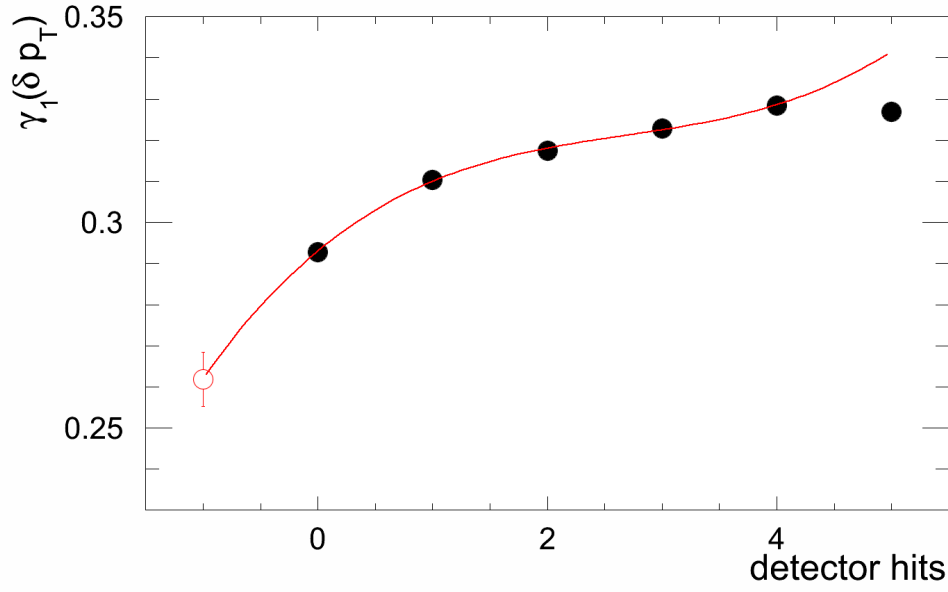
E. Higher Moments

Figure E.1.: Back-extrapolation of the LHC11h skewness $\gamma_1(\delta p_T)$. The measured skewness of $\gamma_1(\delta p_T) = (0.293 \pm 0.001)\,\mathrm{GeV}/c$ is corrected to $\gamma_1(\delta p_T) = (0.262 \pm 0.007)\,\mathrm{GeV}/c$.
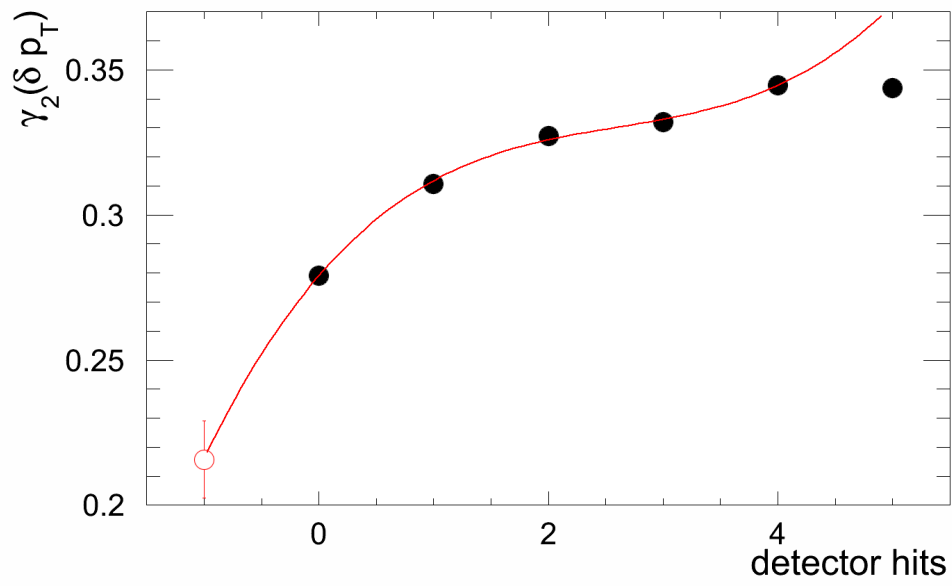
Figure E.2.: Back-extrapolation of the LHC11h kurtosis $\gamma_2(\delta p_T)$. The measured kurtosis of $\gamma_2(\delta p_T) = (0.279 \pm 0.003)$ is corrected to $\gamma_2(\delta p_T) = (0.216 \pm 0.013)$.

F. Back-Extrapolations

All back-extrapolated values for $\sigma(\delta p_T)$, $\gamma_1(\delta p_T)$ and $\gamma_2(\delta p_T)$ are summarized in the following tables. This is done for the simulation, 2010 and 2011 data.

configuration	$\sigma_{\text{sim}}(\delta p_T)$ [GeV/c]	$\sigma_{2010}(\delta p_T)$ [GeV/c]	$\sigma_{2011}(\delta p_T)$ [GeV/c]
simulated	9.458 ± 0.005	-	-
normal	9.449 ± 0.020	11.817 ± 0.026	12.034 ± 0.017
rotating	9.424 ± 0.020	-	-
dependent	9.418 ± 0.020	-	-
exponential	9.423 ± 0.011	11.932 ± 0.024	12.232 ± 0.018
6 points	9.427 ± 0.015	11.723 ± 0.019	11.889 ± 0.013

Table F.1.: All HBOM back-extrapolations for the simulation $\sigma_{\text{sim}}(\delta p_T)$, the 2010 data $\sigma_{2010}(\delta p_T)$ and the 2011 data $\sigma_{2011}(\delta p_T)$ are displayed. The first line "simulated" shows the standard deviation of the simulation without the detector effects. In each line, one configuration is changed from the standard configuration. The standard configuration is the non rotating and independent detector hit with the polynomial fit function using fife points for the fit.
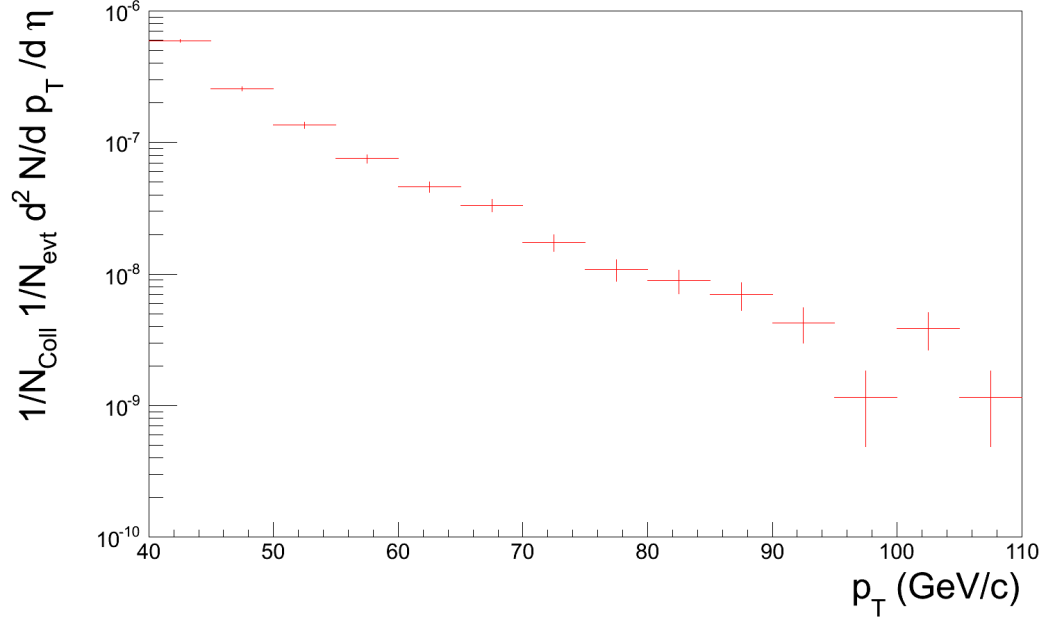
G. 2011 Jet Spectrum

Figure G.1.: Comparison of the 2010 and 2011 jet spectrum. They are obtained with the anti k_t jet finder at $R = 0.3$ and $p_{T,min} = 0.15\,\mathrm{GeV}/c$ at a centrality of $0 - 10\%$. The used Pb-Pb data is available online at [KBb] and [KBd]. The runs are displayed in the appendix in Table B.1 and Table B.2.

Bibliography

[A+08]   K. Aamodt et al. The ALICE experiment at the CERN LHC. *JINST*, 3:S08002, 2008.

[A+11]   K. Aamodt et al. Higher harmonic anisotropic flow measurements of charged particles in Pb-Pb collisions at $\sqrt{s_{NN}}$ = 2.76 TeV. *Phys. Rev. Lett.*, 107:032301, 2011, arXiv:1105.3865.

[A+12a]   Betty Abelev et al. Anisotropic flow of charged hadrons, pions and (anti-)protons measured at high transverse momentum in Pb-Pb collisions at $\sqrt{s_{NN}}$ = 2.76 TeV. 2012, arXiv:1205.5761.

[A+12b]   Betty Abelev et al. Measurement of Event Background Fluctuations for Charged Particle Jet Reconstruction in Pb-Pb collisions at $\sqrt{s_{NN}}$ = 2.76 TeV. *JHEP*, 03:053, 2012, arXiv:1201.2423.

[AKB11]   Anton Andronic and Christian Klein-Bösing. Lecture notes: Introduction to ultra-relativistic heavy-ion collisions.
Westfälische Wilhelms Universität Münster, 2011.

[C+04]   M Cinausero et al. ALICE: Physics performance report, volume I. *J. Phys.*, G30:1517–1763, 2004.

[CS06]   Matteo Cacciari and Gavin P. Salam. Dispelling the N^3 myth for the k_t jet-finder. *Phys. Lett.*, B641:57–61, 2006, arXiv:hep-ph/0512210.

[d'E09]   David d'Enterria. Jet quenching. 2009, arXiv:0902.2011.

[dFKP07]   Philippe de Forcrand, Seyong Kim, and Owe Philipsen. A QCD chiral critical point at small chemical potential: Is it there or not? *PoS*, LAT2007:178, 2007, arXiv:0711.0262.

[Kar02]   Frithjof Karsch. Lattice QCD at high temperature and density. *Lect. Notes Phys.*, 583:209–249, 2002, arXiv:hep-lat/0106019.

[KBa]   Christian Klein-Bösing. 2010 Jet data.
PWGJE Train: Jets_PbPb 31
https://pcalimonitor.cern.ch/trains/train.jsp?train_id=5.

[KBb]   Christian Klein-Bösing. 2010 jet spectrum.
PWGJE Train: Jets_PbPb 26
https://pcalimonitor.cern.ch/trains/train.jsp?train_id=5.

Bibliography

[KBc]   Christian Klein-Bösing. 2011 delta p_T spectrum.
         PWGJE Train: Jets_PbPb_2011 15
         https://pcalimonitor.cern.ch/trains/train.jsp?train_id=16.

[KBd]   Christian Klein-Bösing. 2011 Jet spectrum.
         PWGJE Train: Jets_PbPb_2011 20
         https://pcalimonitor.cern.ch/trains/train.jsp?train_id=16.

[KB11]   Christian Klein-Bösing. Fluctuations Paper and FastMC. Talk held at Jet
         Meeting 2011-08-10, 2011.

[Lef09] C Lefevre. LHC the guide, 2009. CERN-Brochure-2009-003-Eng at
         http://cdsweb.cern.ch/record/1165534?ln=de.

[MOB11] James W. Monk and Cristina Oropeza-Barrera. The HBOM Method for
         Unfolding Detector Effects. 2011, arXiv:1111.4896.

[N$^+$10] K. Nakamura et al. Review of particle physics. *J. Phys. G*, G37:075021,
         2010.

[Rel]   CERN Press Release.
         CERN experiments observe particle consistent with long-sought higgs boson.
         http://press.web.cern.ch/press/PressReleases/Releases2012/
         PR17.12E.html.

[Ron09] F. Ronchetti. The ALICE electromagnetic calorimeter project. *J. Phys.
         Conf. Ser.*, 160:012012, 2009.

[Sal09] Gavin P. Salam. Towards Jetography. 2009, arXiv:0906.1833.

[Ver12] Marta Verweij. Measurement of jet spectra reconstructed with charged
         particles in Pb-Pb collisions at $\sqrt{s_{NN}} = 2.76$ TeV with the ALICE detector
         at the LHC. Analysis note of PWGJE, 2012.
         https://aliceinfo.cern.ch/Notes/node/34.

[Wei07] Christian Weinheimer. Lecture notes: Kern und Teilchenphysik II.
         Westfälische Wilhelms Universität Münster, 2007.

[Zima]   Markus Zimmermann. 2010 HBOM data.
         PWGJE Train: Jets_PbPb_AOD 16
         https://pcalimonitor.cern.ch/trains/train.jsp?train_id=19.

[Zimb]   Markus Zimmermann. 2011 HBOM data.
         PWGJE Train: Jets_PbPb_AOD 15
         https://pcalimonitor.cern.ch/trains/train.jsp?train_id=19.

[Zim10] Markus Zimmermann. Bachelor Thesis: Study of the Response of Different
         Jet-Algorithms for the ALICE-Experiment.
         Westfälische Wilhelms Universität Münster, 2010.

Danksagung

*Hiermit bestätige ich, dass ich diese Arbeit selbstständig
verfasst und keine anderen als die angegebenen
Quellen und Hilfsmittel verwendet habe.*

Münster, 31. October 2012

Markus Zimmermann